face roughness alone. There are, however, an estimated 4×10^{10} m^2 of extremely arid land, 50×10^{10} m^2 of arid land, and 110×10^{10} m^2 of semiarid land within the limits of the contiguous 48 States (ref. 5–11). These relatively undeveloped regions could be the focal point of proposed airborne, Space Shuttle, and spacecraft radar-imaging applications such as the following:

1. Research on development of arid land recreational areas and other aspects of land use.
2. Detection of alluvial deposits for sand and gravel and for water potential.
3. Classification of active sedimentary processes (i.e., monitoring of aeolian activity and defining the extent of silt deposition after floodwaters recede).

Strategic Air Command, X-band (9500 MHz) SLAR images of Death Valley have been acquired recently. A full discussion and comparison of the X- and L-band images will be published in the near future; however, one enlargement of these high-resolution (15 m) X-band data is presented (fig. 5–41) for comparison with specific details on the L-band images.

The conspicuous dark band (unit V) around the base of the gravel fans on the L-band data (fig. 5–31) is present on the X-band image (fig. 5–41), but the area cannot be well delineated because of the less-distinctive tonal contrast between units V and III (the carbonate facies of the outer salt pan). Similarly, the contrast between units III and II on the X-band data is not as sharp as shown on the L-band images.

However, the desert pavement (unit VI) detail is somewhat better on the X-band image because this radar has a higher resolution and a more pronounced shadowing effect. The incident angle of the X-band data in the center of figure 5–41 is 72.3°, whereas the incident angle in the center of the L-band image (fig. 5–31) is 38.2°. The desert-pavement areas are very clearly defined on both radar frequencies as a result of the extremely smooth desert varnish surface (fig. 5–30). The pavement would probably be specular even on K-band images for this reason.

Within the salt pan, the X-band data appear to define geologic contacts between various chloride, sulfate, and carbonate facies differently than the L-band data. However, verification and discussion of the causal relationships must be delayed until further study of the X-band images is completed.

A SHUTTLE RADAR MICROWAVE SUBSYSTEM FOR EARTH RESOURCES APPLICATIONS

Introduction

The microwave subsystem considerations are discussed as a design example for a radar for Earth resources applications to be used in conjunction with the Shuttle Spacelab. This system with a multiplicity of frequencies and polarizations—L-band (25-cm wavelength), S-band (10-cm wavelength), and X-band (3.2-cm wavelength) at two orthogonal linear polarizations—has been tentatively selected. The Space Shuttle vehicle constrains the antenna to approximately 8 m in length and 3 m in width.

The frequencies and antenna size comprise the major constraints on the system described here and determine the sensor altitude, coverage, and major hardware parameters. The sensor performance is summarized as follows:

1. Frequencies:
   a. L-band (25 cm)
   b. S-band (10 cm)
   c. X-band (3.2 cm)
2. Polarization:
   a. Transmit: Vertical or horizontal
   b. Receive: Vertical or horizontal
3. Imagery: Synthetic array; four looks in azimuth; 10-m range and azimuth resolution on the ground.
4. Coverage: Offset of 75 to 275 km either side of the satellite groundtrack.
5. Swath width:
   a. At minimum offset: 40 km
   b. At maximum offset: 100 km

The major microwave subsystem parameters are outlined as follows:

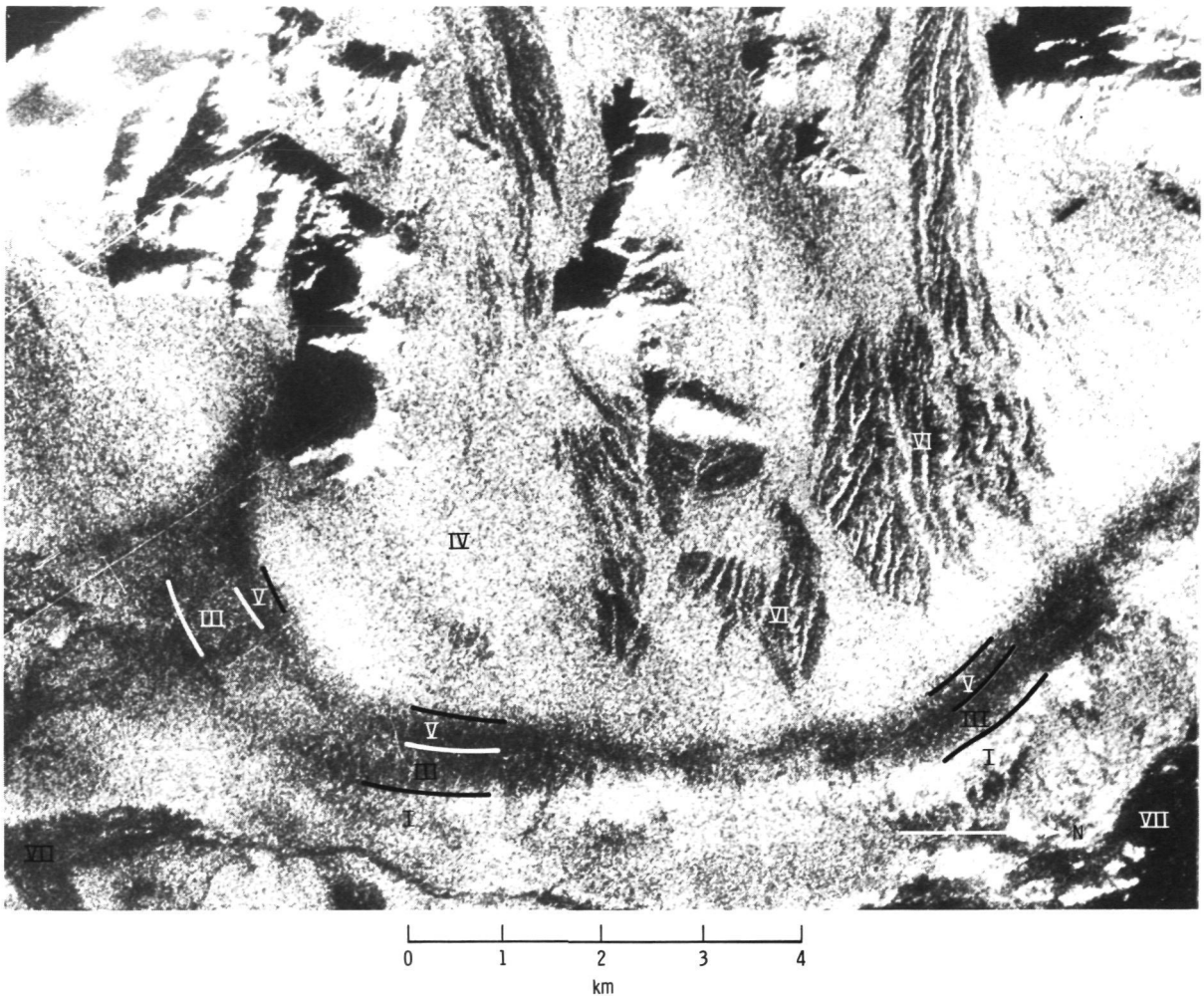

FIGURE 5–41.—Enlargement (10 times) of X-band SLAR image of Tucki Wash Fan. Radar look direction from lower right to upper left; flight altitude, 10 363 m. Compare annotations with figure 5–31. Incident angle (center of image) equals 72.3°, taking into consideration the 2.5° eastward slope of the fan. Dark streaks from upper left to lower right are artifacts of image acquisition. (Strategic Air Command photograph.)

1. Antenna: Dual linear polarization; planar array:
   - *a.* L-band: 2 m high; 8 m long
   - *b.* S-band: 0.75 m high; 8 m long
   - *c.* X-band: 0.25 m high; 8 m long
2. Transmitter: Switchable to either polarization; 2000 pulse/sec:
   - *a.* L-band: Solid state; 60-W average
   - *b.* S-band: Solid state or tube; 200-W average
   - *c.* X-band: Traveling-wave tube (TWT); 600-W average
3. Receiver: Dual channel for both polarizations; parametric amplifier input stage:
   - *a.* L-band: 1-dB noise figure
   - *b.* S-band: 1.5-dB noise figure
   - *c.* X-band: 2.5-dB noise figure
4. Pulse compression:
   - *a.* Chirp: As required to provide acceptable transmitter peak powers and 10-m ground resolution in range for varying offset distances
   - *b.* Off-nadir angle: 45°

To arrive at the design, two limitations must be considered: the antenna aperture constraints (8 by 3 m) on the imagery requirements and the antenna aperture constraints on the antenna design, such as off-track distance requirements, polypolarization, and multifrequency. The approaches to designing optimum transmitters must be considered for the three frequency bands, particularly the X-band transmitter, which requires an average power of approximately 600 W.

The major conclusion concerning the aperture constraint is that the 8- by 3-m aperture imposes a severe limitation on the available swath widths and on the extent of off-track range that is achievable. The maximum achievable offset for the system at an altitude of 200 km is 275 km, and the maximum swath width available at this offset is 100 km. These limitations are described in detail in this section.

Multiple-polarization use of the 8- by 3-m antenna aperture is an important consideration. In this preliminary analysis, the 8- by 3-m aperture was divided into three 8-m strips, each representing a slotted array at L-, S-, and X-bands, respectively, and all having an elevation beamwidth of 12° (fig. 5–42). Reasonable-sized offset ranges and swath widths are attained at all three frequencies.

Radar-power requirements are also fixed when the aperture is divided in the previously mentioned manner. For a signal-to-noise ratio of 15 dB, a 10-m ground resolution is required; and, for a geometric backscattering coefficient of −14 dB, the radiated power requirements for a resolution cell 340 km away are as follows: X-band, 600 W; S-band, 200 W; and L-band, 60 W.

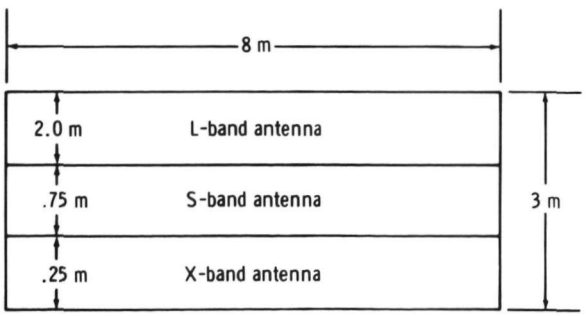

FIGURE 5–42.—Aperture sharing.

System Tradeoffs and Performance

The system tradeoffs considered here determine the radar parameters, PRF, antenna weighting, pulse compression ratio, pulse compression technique, transmitter peak power, and so forth, which draw a desired balance among swath width, available offset ranges, and image quality (given the antenna aperture constraints and transmitter constraints).

At the start of this balancing process, it is necessary to decide how the available aperture is to be shared by the three frequencies and to include dual polarization for each frequency. The 8- by 3-m antenna aperture will be partitioned into three 8-m-long antennas, one each for L-, S-, and X-bands (fig. 5–42). Antenna mechanization is discussed in a subsequent section.

Once aperture sharing is known, the radar PRF, based on the allowable signal-to-ambiguity ratio, can be selected. Also, if the PRF and the antenna elevation pattern are known, the available swath widths and maximum offset range can be determined within the limits of signal-to-ambiguity constraints.

This initial tradeoff process is discussed in the subsections on orbit geometry and on angle ambiguity control and PRF choice. The next section contains a view of image-quality optimization factors that relate to the microwave subsystem. Tropospheric and ionospheric propagation effects are detailed in a separate subsection, which concludes that, from a Space Shuttle altitude of 200 km and at 45° from the vertical, propagation problems are those usually associated with the troposphere (e.g., rain). However, above a 400-km altitude, Faraday rotation by the ionosphere may be an important factor.

Orbital geometry.—The basic geometry associated with a side-looking SAR in orbit around a spherical Earth is shown in figure 5–43. The equations used in determining ϕ,

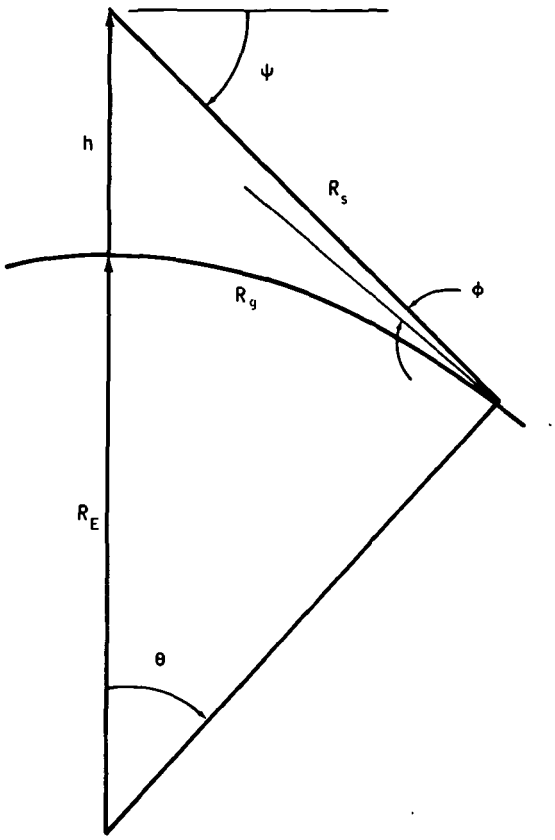

FIGURE 5–43.—Basic orbital geometry of side-looking SAR.

ψ, and R_s as functions of R_g are

$$\theta = \frac{R_g}{R_E} \tag{5–18}$$

where ϕ is the elevation beamwidth, ψ is the depression angle, R_s is the slant range, R_g is the ground range, and R_E is the Earth radius.

$$\psi = \arctan\left[\frac{h + R_E(1-\cos\theta)}{R_E \sin\theta}\right] \tag{5–19}$$

$$R_s = \frac{R_E \sin\theta}{\cos\psi} \tag{5–20}$$

Figure 5–44 shows ϕ, ψ, and R_s as functions of R_g for $h=200$ km. The spherical Earth effects are particularly important at the smaller values of ϕ, where a small change in ψ can cause a large change in illuminated ground range R_g, which makes extremely

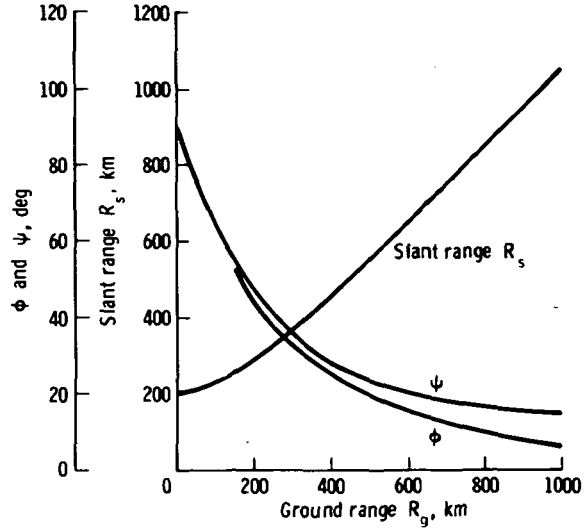

FIGURE 5–44.—Plot of ϕ, ψ, and R_s as functions of R_g ($h=200$ km).

small elevation beamwidths necessary to control range ambiguities.

Angle ambiguity control and PRF choice.—A pulsed radar return spectrum is shown in figure 5–45 for a real antenna with a uniform weighting function. The widths of the returns about each PRF line are independent of the carrier frequency; only the real antenna length l and the vehicle speed v affect the widths.

As the real antenna scans over a point scatterer, the Doppler shift varies and the antenna traverses the regions to be processed as illustrated in figure 5–46. The overlapping

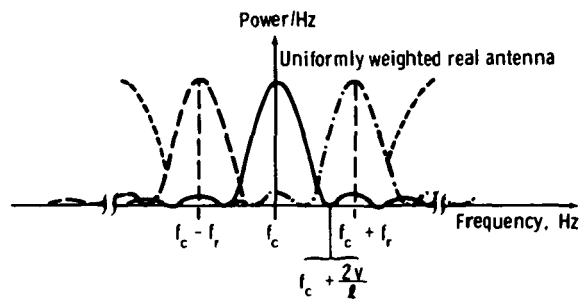

FIGURE 5–45.—Pulsed radar return spectrum for a real antenna with a uniform weighting function (where f_c is carrier frequency and f_r is return frequency).

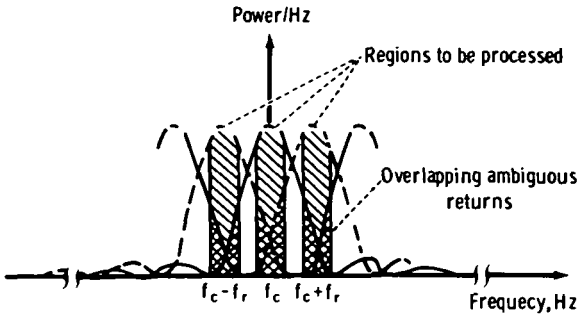

FIGURE 5–46.—Azimuth ambiguities.

returns from adjacent PRF lines are processed simultaneously with the desired returns. The result is an ambiguous synthetic array azimuth pattern. The synthetic aperture azimuth pattern required to hold the azimuth ambiguities to −18 dB is given in figure 5–47. It has been assumed that it is desired to hold the sum of all azimuth ambiguities to −15 dB.

A conservative specification on real antenna, mean, far-out azimuth side lobes $\bar{G}_{SL}$ can be derived as follows. The Doppler frequency extent of the side-lobe region is $\pm 2v/\lambda$. Therefore, the processed region near each PRF return line contains the contributions from $N=4v/f_r$ other PRF lines. At a nominal PRF of $2v/l$, $N=2l/\lambda$. Next, arbitrarily let it be required that the sum of all N contributions be −10 dB relative to the −27-dB peak of figure 5–47; then, the following equation results:

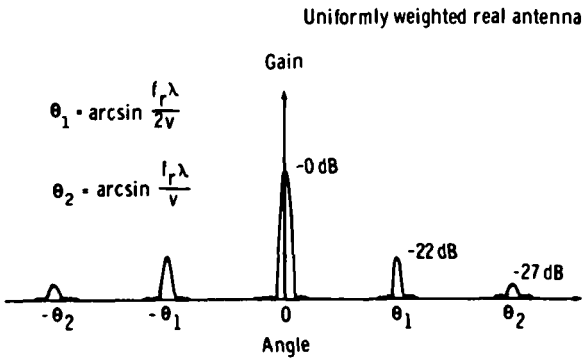

FIGURE 5–47. Synthetic aperture azimuth pattern required to hold azimuth ambiguities to −18 dB.

TABLE 5–X.—*Azimuth Far-Out Side-Lobe Level Requirements*

f_c	N, dB	$\bar{G}_{SL}$, dB
X-band	27	−32
S-band	22	−29.5
L-band	18	−27.5

$$20 \log_{10} G_{SL} + 10 \log_{10} N = -37 \text{ dB} \qquad (5\text{–}21)$$

The resulting requirements on average azimuth side-lobe levels for $l=8$ m are given in table 5–X.

The PRF can be adjusted so that, when it operates with four independent azimuth looks, the worst-case azimuth ambiguities (in the outer two processing regions of fig. 5–48) are −18 dB. For these particular ambiguities, the proper PRF choice is approximately $2v/l$. Similar considerations for three, two, and one azimuth looks yield the PRF as a function of the number-of-looks curve plotted in figure 5–49. The figure also shows $c/2f_r$ (the slant-range distance between transmitter pulses), which is an important measure of ground-range coverage, as shown in the following section.

Range ambiguity control and ground-range coverage.—From the previous section, it is noted that $c/2f_r < R_s$. Thus, many range am-

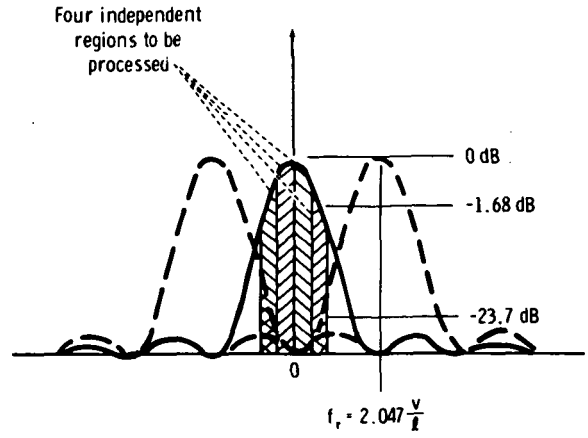

FIGURE 5–48.—Azimuth ambiguity adjustment for four independent azimuth looks.

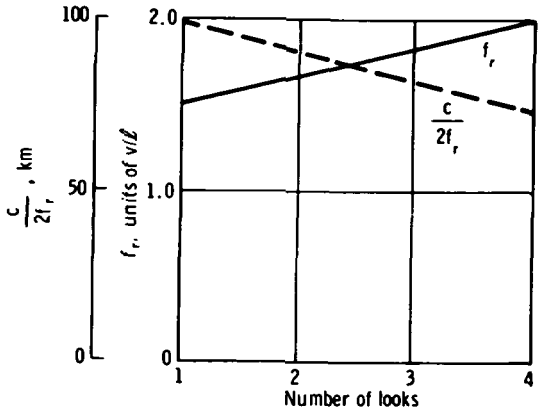

FIGURE 5–49.—The PRF and interpulse slant range compared with number of looks.

biguities will result unless the antenna elevation pattern is used to reject undesired returns (fig. 5–50). The ambiguous ranges are kept in the side lobes of the real antenna elevation pattern. Figure 5–51 illustrates the situation for smaller depression angles; a

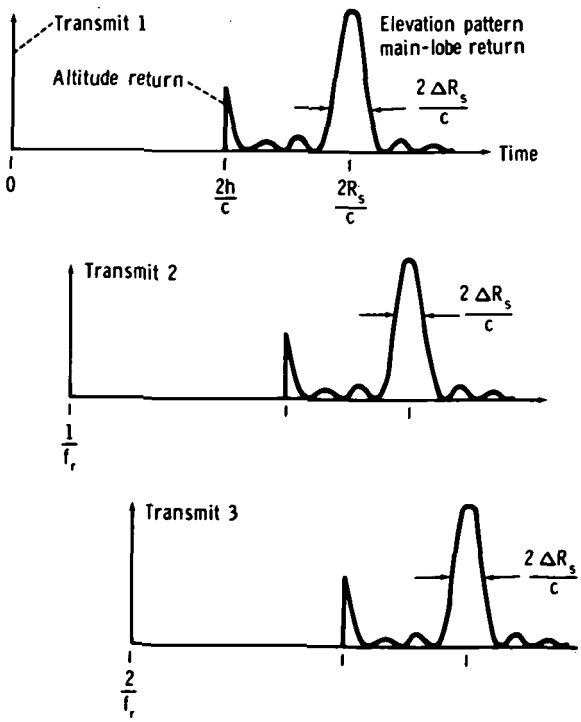

FIGURE 5–50.—Range ambiguity control (large depression angle).

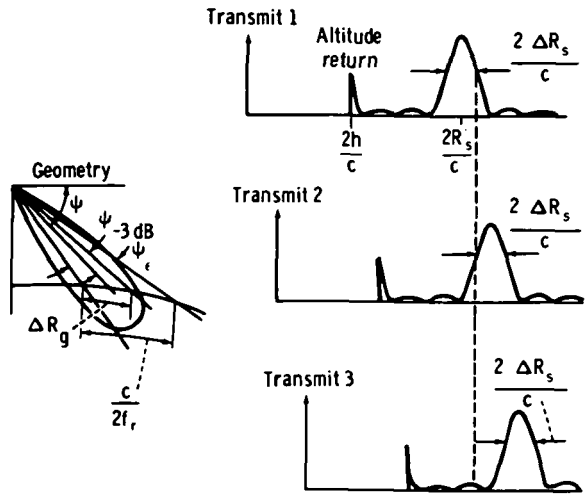

FIGURE 5–51.—Range ambiguity control (small depression angle).

given elevation beamwidth covers a greater slant range than before. Thus, to realize the maximum coverage from a given PRF choice, the real antenna elevation beamwidth must become a function of depression angle (or of ground range). The PRF should be adjusted as a function of altitude and antenna elevation pointing angle to cause the altitude returns to fall outside the desired range coverage. A small compromise in angle ambiguity level or in range coverage may be required at certain combinations of altitude and elevation pointing angle.

To estimate elevation beamwidth requirements and to estimate ground-range coverage, it was assumed that the elevation aperture of the real antenna is uniformly weighted and that the worst-case range ambiguities (at the edges of the range coverage) must be −18 dB relative to the desired returns at the edges of the range coverage. As before, the −18-dB figure was determined by interpreting the −15-dB specification to apply to the sum of all ambiguities.

Figure 5–52 shows the power return as a function of time for the following conditions: The worst-case range ambiguities (−18 dB) are present, the elevation aperture is uniformly weighted, and the ground-range coverage is that encompassed by the −3-dB one-

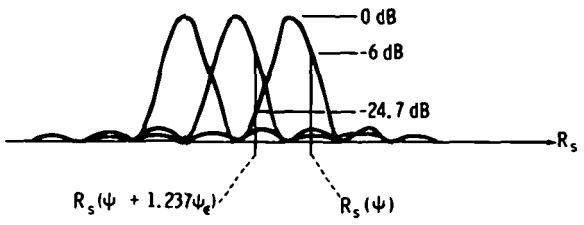

FIGURE 5–52.—Antenna elevation pattern adjusted for −18-dB range ambiguities.

way elevation pattern $\psi_{-3\ dB}=0.443\psi_\epsilon$. It can be shown that

$$\frac{c}{2f_r}=R_s(\psi+\psi_\epsilon)-R_s(\psi-\psi_\epsilon) \qquad (5\text{–}22)$$

$$\Delta R_g=R_s(\psi+0.443\psi_\epsilon)-R_s(\psi-0.443\psi_\epsilon) \qquad (5\text{–}23)$$

The results plotted in figure 5–53 can be derived from these two equations. This figure is for the case in which the real antenna elevation is continuously adjusted to optimize the ground-range coverage, limited only by the ambiguity levels previously discussed. Antenna design problems, radar power output, and elevation pointing accuracy problems have been ignored to show that the maximum theoretical limits are under only the ambiguity constraints.

Good coverage is still possible for a single elevation angle. Figure 5–54 shows three discrete coverage zones obtained at an altitude of 200 km from a real antenna elevation beamwidth of 12°.

As a trial design, the aperture constraints assumed were (1) that the 3-m vertical aperture available was shared among X-, S-, and L-bands without physically overlaying the antennas, and (2) that the elevation beamwidths of the three antennas were equal. These assumptions resulted in three antennas, each 8 m long, having vertical apertures of 0.25, 0.75, and 2.0 m at X-, S-, and L-bands, respectively. The elevation beamwidths of the three antennas are 6.4° minimum and are weighted to generate the 12° beam.

A conservative specification on real antenna far-out elevation side lobes can be derived as follows. The slant range extent of the side-lobe region is $R_{s_m}-h$, where R_{s_m} is the slant range to the horizon. The maximum number of range ambiguities is

$$M=\frac{R_{s_m}-h}{c/2f_r} \qquad (5\text{–}24)$$

At a nominal PRF of $2v/l$ and with $l=8$ m, $c/2f_r=76.9$ km; thus, $M=18.3$. Next, arbitrarily assume the requirement that the sum of all M contributions be −10 dB relative to the −24.7-dB level of figure 5–52. The following equation is the result:

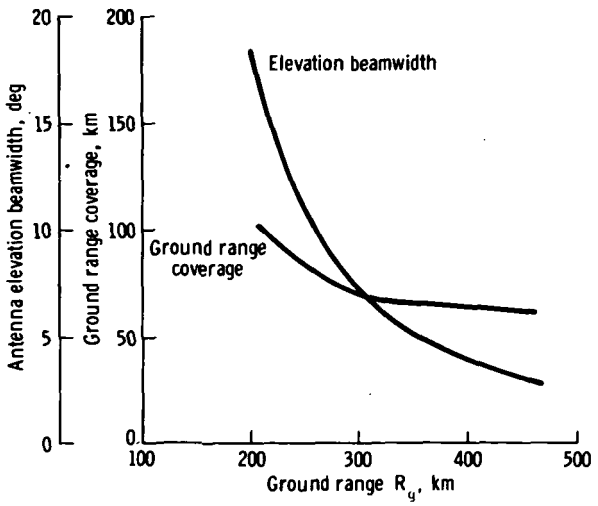

FIGURE 5–53.—Ground range coverage and antenna elevation beamwidth as a function of ground range (ambiguity constraints only); $h=200$ km, $l=8$ m, $f_r=2.047$ v/1, four azimuth looks.

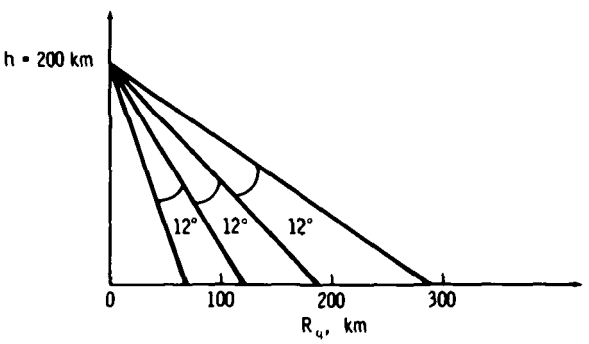

FIGURE 5–54.—Ground range coverage with one elevation beamwidth.

$$20 \log_{10} \bar{G}_{SL} + 10 \log_{10} M = -34.7 \text{ dB} \qquad (5\text{–}25)$$

The resulting requirement on average elevation side-lobe level is $\bar{G}_{SL} < -23.7$ dB.

Image-quality performance.—For the final radar design, a complete resolution and side-lobe budget to allocate all error sources must be developed to specify tolerances throughout the system so that overall performance requirements can be met. Some typical error sources for the transmitter/receiver section are described below.

The dominant contributors to integrated side lobes by the transmitter/receiver are (1) quadratic phase errors between the transmitted pulse and the pulse compression decoding signals, and (2) amplitude ripples across the transmitted pulse.

Figure 5–55 shows the effect of quadratic phase error for cosine-on-a-pedestal weighting functions defined by

$$h(x) = \frac{1 + 2F \cos x}{1 + 2F}, \qquad -\pi < \chi < \pi \qquad (5\text{–}26)$$

where x is the phase difference between transmitted pulse and the decoding signals and where the main beam broadening factor

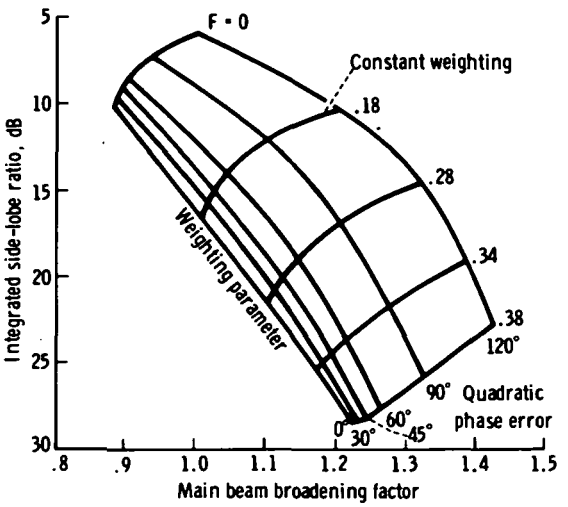

FIGURE 5–55.—Resolution effects of quadratic phase error on integrated side-lobe ratio and main beam broadening.

F is 0.886 for a uniformly weighted compression filter. For example, this figure shows that for a designated parameter (given an integrated side-lobe ratio (ISLR) of 27 dB and a broadening factor of 1.2 with no quadratic phase error), the effect of 30° of quadratic phase error is to degrade the ISLR by 0.5 dB and to degrade the resolution by approximately 1 percent.

Amplitude ripples are caused by ripples across the transmitter bandpass and by ripples on the modulating pulse. A ripple of ±1.5 percent produces two −42-dB side lobes.

For performance in the azimuth dimension, similar criteria apply, except that these criteria are now applied on a pulse-to-pulse basis. Thus, pulse-to-pulse coherence must produce short-term (over an array time) quadratic phase errors of less than approximately 30°. Random-phase errors result in an ISLR equal to the variance of the phase error (in radians). For example, a standard deviation of random-phase errors of 0.02 radian results in an ISLR of −34 dB.

Propagation effects.—In the formation of a synthetic array map from an orbital platform, the radar signal traverses both a portion of the lower ionosphere and the troposphere. The free electrons in the ionosphere cause the index of refraction to vary in time and space. In addition to being dispersive, the medium is doubly refracting, producing a Faraday rotation of a linearly polarized wave. The random fluctuation in index induces random-phase errors on the signal.

The index of refraction in the troposphere also varies in time and space, principally because of varying amounts of water vapor. However, the index is not frequency dependent; thus, the medium is not dispersive. In addition to inducing random-phase errors on the signal, the troposphere may contain precipitation that produces attenuation and backscatter, which are frequency dependent.

For a radar-platform altitude of 200 km, it is found that (for a rather severe ionospheric electron density profile) the Faraday rotation is less than 1° (two way) at 1 GHz, decreas-

ing as f^{-2} with increasing rf. Phase errors resulting from the ionosphere are estimated to be negligible (as is the dispersive effect) for frequencies above 1 GHz.

Tropospheric-induced phase errors are also found to be negligible at a 10-m resolution for any frequency below 10 GHz. The only serious propagation effect is found to be that caused by precipitation in the lower troposphere. Warm-front rain can produce backscatter so that barren ground ($\sigma^\circ \approx 10^{-2}$) will produce an echo less than 15 dB above the precipitation echo at frequencies above 6 GHz. Thunderstorms produce the same limitation at frequencies above 2 GHz, but they are much less common.

If the radar altitude is increased, the Faraday rotation is the only effect that changes materially. For the electron-density profile that produces less than a 1° round-trip rotation at 1 GHz and a 200-km altitude, the Faraday rotation increases to approximately 10° at a 400-km altitude, assuming the same off-nadir angle. This increase may begin to affect the dual-polarization signature information needed for surface classification (e.g., crop identification).

Probably, only precipitation will produce a significant tropospheric effect. It will occur at the upper end of the 1- to 10-GHz band.

Hardware Discussion

The hardware aspects of the microwave subsystem, antenna, transmitter, receiver, exciter, and pulse compressor are discussed in this section. The antenna and transmitter are the critical items in a satellite radar; the antenna is critical because of its large size, and the transmitter is critical because it is the major consumer of prime power and the unit in which the greatest voltage and current stresses occur. Therefore, these two units are covered in more detail than the receiver, exciter, and pulse compressor, which do not exhibit any major problems in the transition from airborne to satellite radars.

Antenna design considerations.—This antenna discussion is divided into three areas: antenna requirements, general design problems, and a candidate design. The various system requirements, frequencies, polarizations, and so forth, are examined with respect to their effect on antenna design and performance. Typical design considerations, which include multiple-frequency band operation, rf and signal bandwidth, manifolding, multipacting, and aperture phase tolerances, are discussed. A possible approach that has potential for satisfying the basic requirements is presented.

Antenna requirements: The necessary radiation pattern performance in both the azimuth and elevation directions is determined by the permissible level of interference contributed by ambiguities. With the elevation pattern, sufficiently steep sides and low side lobes at certain angles are required to avoid interference in the range interval of interest from multiple-time-around returns, near-in returns (particularly the altitude line), and the returns for the same range on the opposite side of the vehicle. The azimuth pattern must provide a sufficiently low side-lobe level to avoid undue contribution to interference from the integrated ambiguities. The required performance depends on the overall system design because some contributions to interference can be avoided by other means; for example, the altitude line can be moved with a small change in rf.

In general, the more complex the antenna becomes in terms of polarization flexibility or multiple-frequency operation within the same aperture, the more difficult it will be to provide precise control of the pattern shape and side lobes. With a single polarization and operation in a single-frequency band, rms side-lobe levels (beyond the first few) of approximately 45 dB below the main beam gain can be expected. However, if one antenna is interleaved or overlaid with another at a different frequency or polarization, 30 dB may be difficult to achieve. From preliminary system considerations (see section entitled "Angle Ambiguity Control and PRF Choice"), the requirements on the levels of side lobes beyond the first two do not appear severe in either principal plane. Azimuth

side lobes of 32 dB down and elevation side lobes of 24 dB down appear adequate.

An rf bandwidth of approximately 1 percent within a particular band to accommodate some flexibility in the location of the instantaneous bandwidth should not pose difficulty. An instantaneous bandwidth of perhaps 20 MHz, depending on resolution, requires careful attention because the requirement applies not only to the pattern and its variations with frequency, but equally to the phase and amplitude transfer characteristics from the electromagnetic field at points in the far field of the antenna to the current and voltage at the output terminals.

The provision of simultaneous reception on two orthogonal polarizations, while transmitting on one, imposes significant complexity. The degree of orthogonality required of the antenna would be a function of the required experiments (within the constraints imposed by Faraday rotation).

Obtaining polarization diversity concurrent with operations at widely separated frequency bands (greater than an octave) from a single aperture is not deemed feasible if delicate side-lobe and pattern control is needed. Use of separate antennas and radars appears to be the most practical approach; hence, the degree of commonality between designs and the ease of scaling are important considerations.

Design tradeoffs: The previously mentioned considerations pose many problems. Among the design considerations included are tolerance effects, pattern and polarization considerations, and multipacting effects.

Aperture phase tolerance: The problem of maintaining aperture phase tolerances is associated with antennas that are electrically long with respect to a wavelength. Failure to maintain phase tolerance results in increased side-lobe levels, filling in of the nulls, and, to a lesser extent, decreased gain. Errors in the excitation of the antenna can result from either electrical causes or mechanical distortions. The effects on the radiation pattern are indistinguishable. The error budget must be allocated between electrical and mechanical causes. Thermally induced distortions can be particularly severe when illumination of the antenna by the Sun is possible from many directions. However, numerous methods exist to deal with this problem. The antenna may be partially isolated from the heat source (the Sun) by a cover. The thermal coefficient of expansion may be minimized by use of materials such as graphite-fiber-reinforced plastics, which have been applied for communication spacecraft antennas. Another possible solution is the use of very high thermal conductivity materials that minimize temperature gradients. Still another partial solution is to use mesh structures that have high optical transparency.

In general, the errors in the antenna that cause degradation of the pattern can be divided into three classes, depending on their distribution over the radiating aperture:

1. Slowly varying systematic errors along the antenna caused by factors such as bending of the main support structure.

2. Errors associated with groups of elements caused by positional errors in mounting and phase and amplitude errors in the excitation of the feed manifold.

3. Small-scale random errors associated with the individual elementary areas of the antenna.

Elevation pattern: Assuming that mapping on either side of the Space Shuttle is desirable, two beam types can be considered: (1) a symmetrical beam (with respect to the Space Shuttle elevation plane) that requires the vehicle only to be rolled to map similar swaths on either side, and (2) a shaped or asymmetrical beam that requires the vehicle to yaw 180° to map an identical swath on the opposite side. This comparison is illustrated in figure 5–56.

Azimuth side lobes: Aperture distribution tapering may prove desirable in the azimuth plane to reduce side-lobe clutter contribution within a range ring. Standard Taylor distributions could then be used to optimize gain for the given side-lobe level. Only a moderate

increase in feed complexity will result from such tapering of the aperture distribution.

Polarization diversity: Polarization diversity creates a severe design problem that requires ingenuity for its solution; it complicates the design to the extent that very wide band performance is impractical.

The candidate design is configured to provide two orthogonal, linearly polarized antenna patterns with separate output ports for each polarization. Thus, received orthogonal signals can be processed individually in accordance with the particular experiment. Transmission can be accomplished on either polarization with appropriate switching in the transmitter. Furthermore, by dividing the transmitter output between the two linear antennas with the proper phase relationship, circular polarization can also be obtained. If done electronically, these switching schemes can be relatively complex. It may be worthwhile to consider in-flight adjustment or component substitution to simplify the design.

Multipactor effects: The operation of rf devices in the vacuum environment of space presents the microwave engineer and designer with electrical breakdown problems, which can be more serious than those caused by ionized discharge. The problem arises because the mean free path of electrons in the space environment may be larger than the dimensions of the rf components. Under such conditions, a secondary emission resonance (multipacting) may occur. Multipactor discharge is not necessarily a high electric field phenomenon; components operated at rf power levels as low as 1 W, when the frequency is greater than a few tens of megahertz, are susceptible. The problem is familiar to designers of microwave tubes; however, the need for designers of other active microwave devices to focus attention on the subject became evident only when suspected multipactor failures occurred in space probes.

Candidate antenna design: A strong candidate and one of the most straightforward designs for the type aperture contemplated

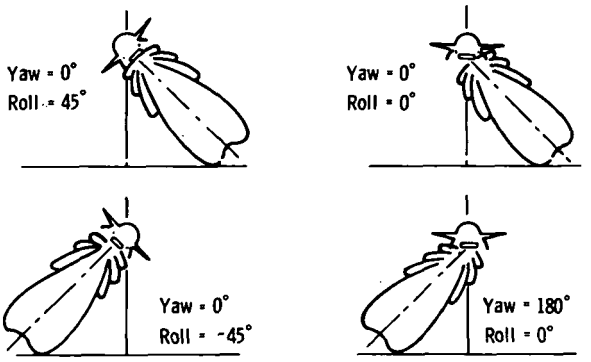

FIGURE 5–56.—Elevation pattern coverage.

is illustrated in figure 5–57. The design is the planar array of waveguide slots that produces linearly polarized radiation with the direction of polarization of the electric field parallel to the long dimension of the array. The slots used for this design are displaced shunt slots in the broadwalls of identical parallel guides. Each guide is the required length to form the proper beamwidth at the frequency of operation. The arrangement of slots along each waveguide can be designed to generate a phase and amplitude distribution that causes shaped beam or low side-lobe patterns, if either is desired.

An X-band planar array antenna designed for a space application is shown in figure 5–58. The array is 7.7 m long and 1.23 m high. The array has a structural backing that (1) supports the radiating panels that form the aperture, (2) provides support and attaching points for the waveguide corporate feed that

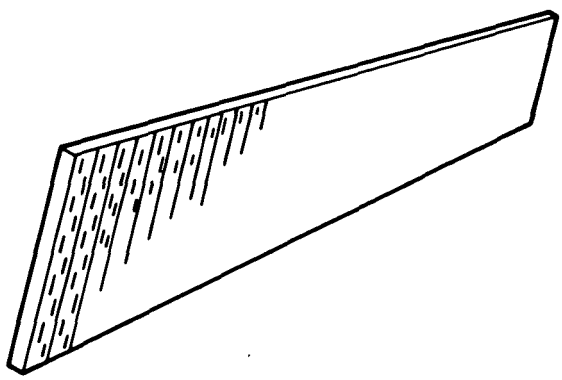

FIGURE 5–57.—Linearly polarized slotted array.

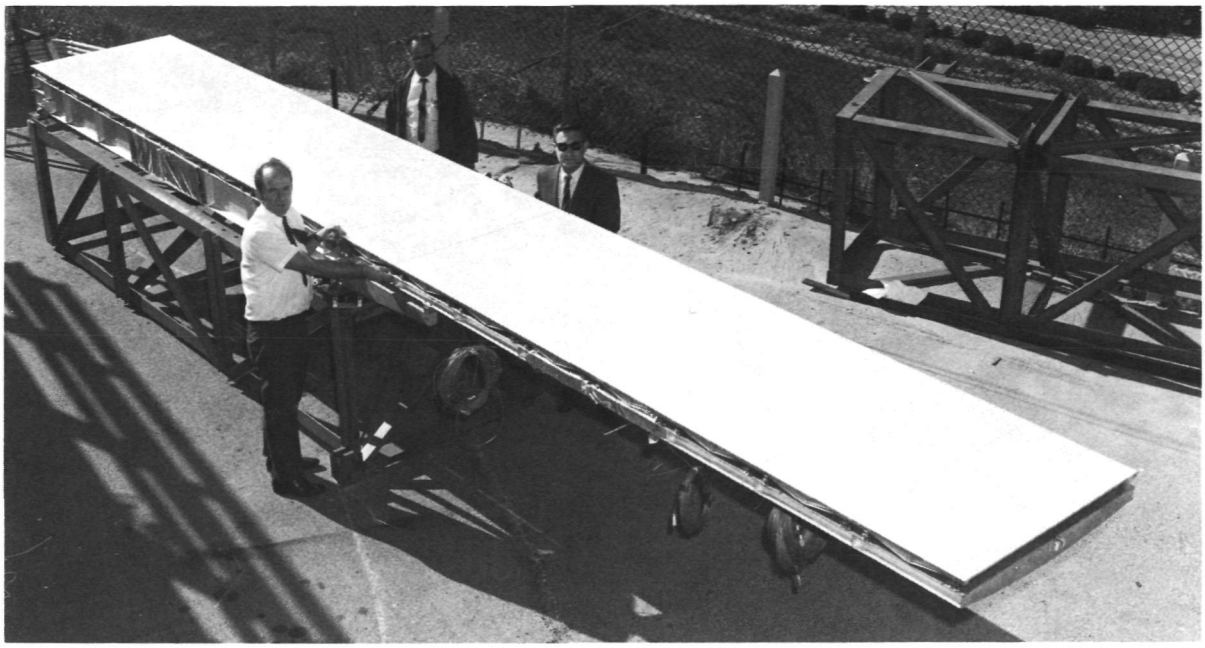

FIGURE 5–58.—An X-band planar array antenna.

distributes power to the array, and (3) protects the array and feed from uneven thermal radiation that would otherwise cause intolerable amounts of physical distortion. The array has been built and tested electrically. Environmental testing, including static tests, vibration tests, and thermal tests, was performed successfully.

Extension of the basic array design described previously yields a design that operates with two orthogonal orientations of linear polarization in which a second array is added. This addition can be accomplished in several ways; the most direct way is to add a second array in front of the first. The front array, if constructed with waveguides that use inclined shunt slots on the guide edges, can be overlaid on the rear array with spaces between the waveguides that allow the rear array to radiate unimpeded through the structure of the front array. This design is shown in figure 5–59.

Transmitter design considerations.—The transmitter designer must choose between solid-state and tube-type transmitters. For the average powers under consideration (X-band, 600 W; S-band, 200 W; and L-band, 60 W), the X-band transmitter will almost certainly be a tube type; the L-band transmitter will almost certainly be solid state; and the choice for the S-band transmitter will require additional study. Considerations affecting the choice of tube or solid-state transmitters for the satellite radar are discussed in this section.

Solid-state power amplification: As single sources of high rf power, vacuum tubes are presently secure in their transmitter role. At the lower frequencies, for which solid-state amplification is more efficient and opportunities exist for effectively combining the outputs of several devices, the solid-state approach may offer performance competitive with or superior to that of the tube. Therefore, an evaluation of high-power solid-state transmitter configurations implies consideration of both of the devices and the methods of power accumulation.

Solid-state devices: Three important classes of solid-state devices for the generation and/or amplification of microwave power are transistors, transferred electron devices (TED), and avalanche transit-time devices. The modes of operation, although

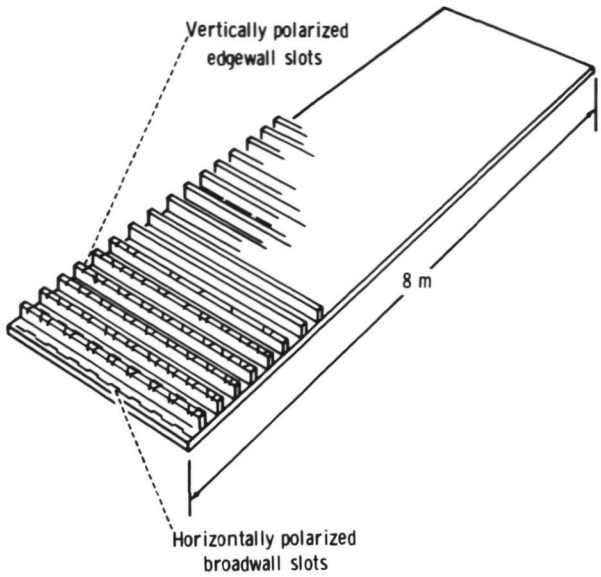

FIGURE 5–59.—Dual-polarized waveguide slot array concept.

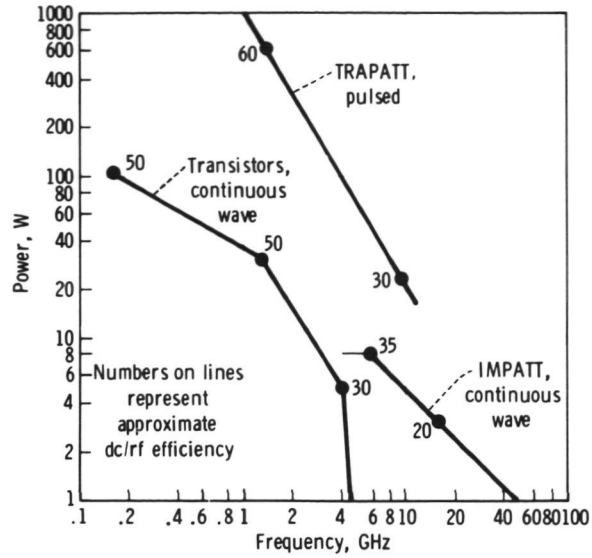

FIGURE 5–60.—Power capabilities of solid-state devices.

considerably different among these classes, have some common characteristics. A prime characteristic is the common requirement for relatively low operating voltages of less than 100 V, depending on the frequency and power desired. A second, less-desirable characteristic is the average power-output limitation caused by thermal effects in which a single device is limited roughly to the 10- to 100-W range, depending on thermal resistance of the design. The present power capability of single devices is shown in figure 5–60. Higher power can only then be obtained through a combination of these devices. The applicability of these devices is summarized in table 5–XI.

The rf power accumulation: When more microwave power is required than can be provided by a single solid-state device, accumulation techniques must be used. These techniques are divided into three areas following the natural interface breakdown of modern systems. Each area is considered independently in the following discussion.

First, there is the combination of devices or chips within a single package. Researchers have shown that both series and parallel techniques are feasible and result in substantial power improvements. Parallel thermal mounting results in increased heat dissipation, whereas interconnection flexibility allows control over impedance levels. This method has the most potential for power/cost improvement because of the applicability of multiple-chip processing on a common heat sink. Mounting circuit complexity may even

TABLE 5–XI.—*Summary of Solid-State Source Candidates*

Device	Appraisal
Transistors	Strong contender below 4 GHz.
TED	Not recommended because of low power and efficiency.
TRAPATT [a] devices.	High peak powers for moderate-to-low pulse widths (<10 μsec) and low-duty factors <1 percent; possible use depending on system final requirements.
IMPATT [b] devices (GaAs) [c].	Moderate efficiencies 20 to 30 percent; highest average power above 4 GHz.

[a] Trapped plasma avalanche triggered transit.
[b] Impact avalanche transit time.
[c] Gallium arsenide.

be reduced if impedance changes result in easier match requirements. Perhaps, 9 to 12 devices will be an optimum number connected in a series-parallel arrangement, mounted on a diamond heat sink.

After maximizing the power from a single package, the next step is to combine packages within a single component. This step is more difficult because distributed effects begin to have an important role. Linear techniques are usually limited to a low number of packages (three to four) due to interaction and power saturation in the downstream devices. Presently, radial configurations appear to have more potential (using symmetry for circuit stability and maintaining equal phase and power levels at all devices).

The third area of power accumulation is concerned with combining the outputs of various independent amplifiers or oscillators to sum the power, while maintaining stability and minimizing circuit losses. Spatial accumulation (or combining in space as is done with multielement radiators) acts independently, using spatial interference to produce the desired summation. This technique can only be used when it is necessary to have all the power available at one port or terminal. Otherwise, circuit accumulation must be used. Usually, hybrids or two-way Wilkinson circuits are used for this purpose. Although both circuits supply the necessary isolation between the power components, they are only two-way circuits requiring n stages of accumulation (2^n-1 combining circuits) for 2^n power components, which is cumbersome and impractical where $n \geq 4$.

Reliability: The chief advantage of solid-state devices in this application is in their improved reliability over vacuum-tube transmitters. Solid-state devices, in general, have demonstrated the capability of long life under normal operating temperature ranges, such as 473 K, at the junction. Elevated junction temperatures are common, however, for high-power devices, and result in reduced expected lifetime. A tradeoff is necessary to balance the mean time before failure (MTBF) with the power required for each device. An example of this relationship is shown in figure 5–61 for silicon IMPATT devices. As indicated, temperatures approaching 573 K are to be avoided because the lifetime is reduced sharply.

A related aspect of reliability is the failure mode of a system. If all the rf power is generated by a single device, its failure forces a system failure. However, when many devices are integrated to supply the necessary power, failure of some of the devices will only reduce the system capability. In fact, an increase in system MTBF may be obtained by a slight overdesign on the number of devices required. A 20-percent increase in devices will increase the system MTBF by a factor of 100 (fig. 5–62).

Tube transmitter: The major tradeoffs required for the definition of tube transmitters lead to—

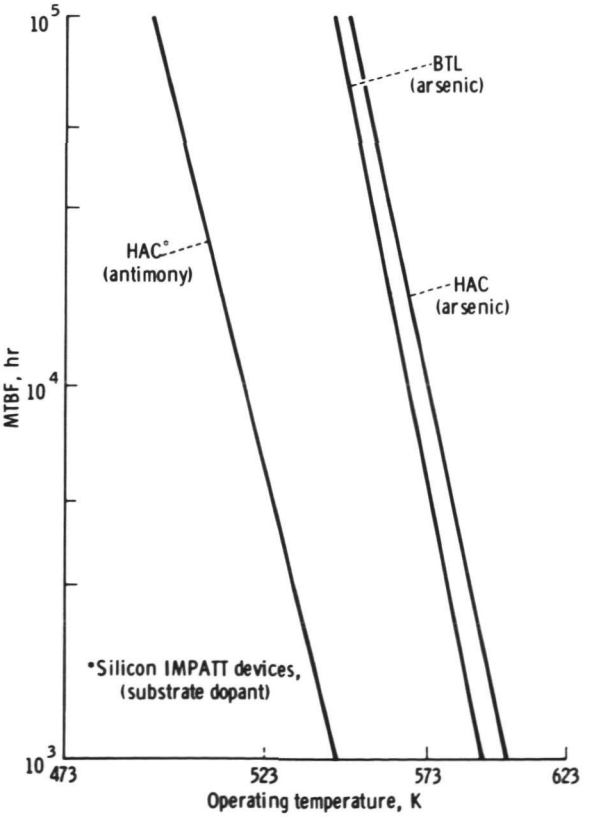

FIGURE 5–61.—Life expectation of silicon IMPATT devices related to junction temperature. Silicon IMPATTS. Hughes Aircraft Corp. (HAC), Bell Telephone Laboratories (BTL).

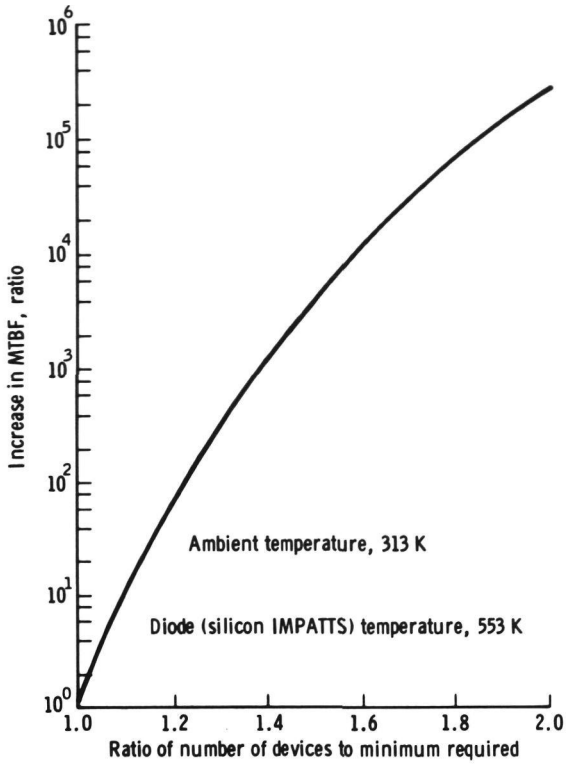

FIGURE 5–62.—Improvement of MTBF through redundancy of solid-state devices.

1. Choice of power amplifier tube.
2. Definition of high-voltage power and modulator circuits.
3. Selection of high-voltage medium and interconnection techniques.
4. Specification of high-power microwave components.
5. Mechanization of the control and monitor functions.

The average power levels range from approximately 60 W at L-band to 600 W at X-band. Using a PRF of 2000 Hz and a compressed pulse width of 0.05 μsec as nominal values and assuming that the duty cycle is not limited by swath width and corresponding listening-time requirements, the duty-cycle values corresponding to pulse-compression practical limits of 1 (no compression) and 2500 are 0.0001 and 0.25, respectively. Average power and corresponding peak-power limits for these and intermediate-duty cycles are shown in figure 5–63.

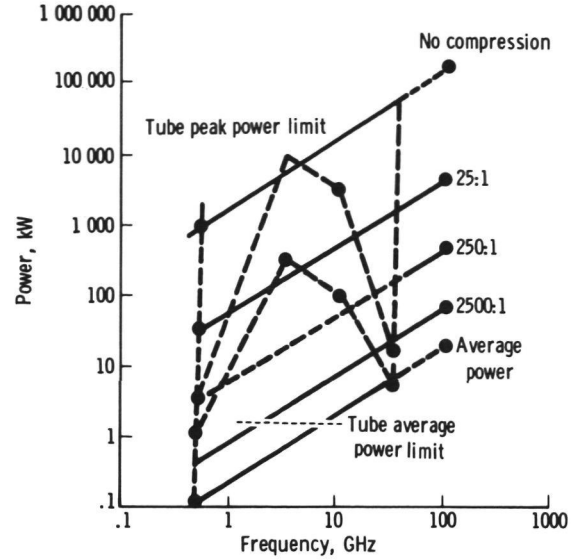

FIGURE 5–63.—Average and peak power transmitter requirements.

Also shown in this figure are average- and peak-power limits of existing high-reliability tube technology. A minimum bandwidth of 100 MHz is assumed to permit frequency agility. This bandwidth requirement excludes all tubes, except the TWT and crossfield amplifiers (CFA), below 5 GHz. Above 5 GHz, the broadband klystron (2 percent bandwidth) is a usable candidate. At the very lowest frequencies, the TWT is usually peak-power-limited by practical length and weight restrictions. At the higher frequencies, all linear beam tubes and the crossfield devices are both peak- and average-power-limited by focusing problems and the low thermal capacities of the small rf circuit structures that intercept the electron beam.

It is generally recognized that the sources of most failures in high-power transmitters are the high-voltage circuits and the critical tube interfaces. High-voltage power supplies at the 10-, 20-, and 30-kV levels, with peak powers as much as 100 kW and average powers to 1 kW, have been developed for space application. The tube-interface problem has also been addressed with the development of very simple pulse modulators, fail-safe bias supplies, and internal control-monitor circuits that limit the pulse width and duty

cycle and, in the event of a detected fault, automatically command the transmitter to a safe mode.

The rf breakdown at low-pressure levels by ionization of residual gases or by multipacting is a source of transmitter failure even in moderate rf power circuits. Both problems may be solved by use of pressurized rf lines or by a carefully designed and fabricated vacuum assembly.

The vented or vacuum approach requires control of the rf fields and element spacings to eliminate all low-order multipactor modes and choice of materials with low secondary-emission coefficients. In the vented approach, outgassing must be limited to prevent ionization breakdown, which implies choice of suitable materials and isolation of all surfaces from contamination during the extended test activities between manufacture and completion of launch.

The choice of high-voltage insulation, modulator circuits, rf duplexing and switching elements, and the detailed mechanization of the monitor and control unit will all depend on the power level of the transmitter. For the lowest power levels, a solid dielectric high-voltage insulation is advantageous. For higher power levels involving increased thermal losses, solid dielectrics are sometimes damaged by differential expansion, and the choice of a gas or an oil dielectric is preferred.

Similarly, a low-duty-cycle single-waveform transmitter using a TWT, klystron, or CFA may efficiently use a line-type cathode modulator, whereas a requirement for waveform flexibility would indicate the use of a tube modulation electrode, such as a mode anode, aperture grid, or shadow grid in combination with appropriate bias and modulation waveform coupling circuits.

Receiver design considerations.—The major element of receiver design for the Space Shuttle is low noise to minimize transmitter power requirements. A plot of noise figure as a function of frequency is shown in figure 5–64 for various solid-state-receiver front-end candidates, including balanced mixers,

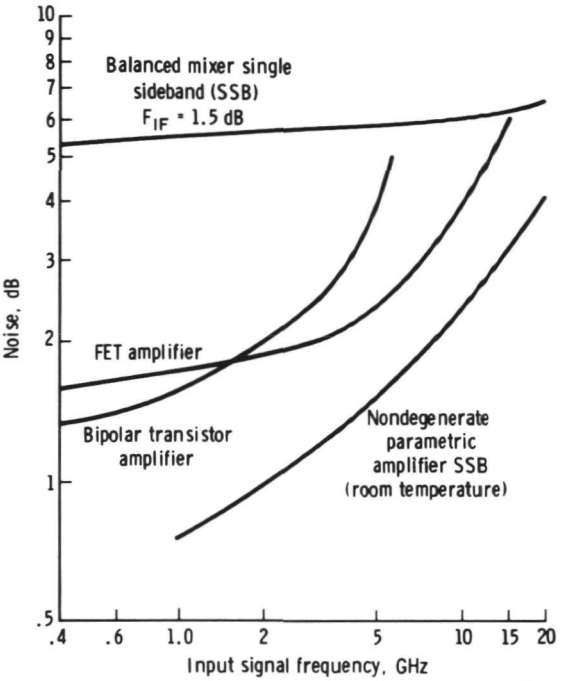

FIGURE 5–64.—Receiver front-end noise performance as a function of frequency.

transistor amplifiers, field-effect transistor (FET) amplifiers, and parametric amplifiers. Although noise figure is an important characteristic to the system designer, other characteristics, such as bandwidth, dynamic range, gain, reliability, and cost, must be considered.

The balanced mixer can be designed and fabricated in almost any form (stripline, waveguide, or microstrip) and can be designed in a single- or double-balanced configuration. Designs vary from 10 percent to multioctave bandwidth. These devices commonly employ Schottky barrier diodes for low noise and high reliability. The dynamic range of the mixer is a function of the diodes and the local oscillator (LO) power level. With local oscillator power in the 10-mW range, the two-dioxide mixer exhibits a 1-dB signal compression at an input level of approximately 3 dBm. It is possible to terminate the image port in the mixer and obtain a 1- to 2-dB noise figure improvement. The penalty is a reduction in bandwidth and a considerable increase in circuit complexity.

Low-noise bipolar transistor amplifiers are relatively simple and can be fabricated in stripline or microstrip. The design techniques are mature; and, with available devices, octave bandwidths are feasible. The gain per stage varies from 20 dB at 400 MHz to 7 dB at 6 GHz. For a 20-dB gain amplifier, 1 dB of gain compression typically occurs at a 5- to 10-dBm output.

Considerable effort is being expended on gallium arsenide (GaAs) FET amplifiers. The noise figures shown on figure 5–64 are presently available in the laboratory; however, commercial devices are available with a 5-dB noise figure and an 8-dB gain at 8 GHz. Amplifiers can be constructed in coaxial or microstrip and are capable of a 10-percent bandwidth. Typically, 1-dB gain compression occurs at a 10-dBm output. Device-reliability data are not presently available.

The parametric amplifier is the most complex of the practical spacecraft front-end candidates, but it offers the lowest noise figure. Amplifiers presently used in airborne radar systems use one or two varactor stages and have signal bandwidths from 3 to 10 percent and gains of 15 to 20 dB. The pump power and frequency requirements depend on operating frequency and required noise figure. Typical levels are 20 to 100 mW in the frequency range from 12 to 50 GHz. The Gunn diode oscillator can easily meet these requirements. The parametric amplifier is further complicated by the necessity for maintaining the temperature at or below room temperature. Typically, 1-dB gain compression occurs at a −35-dBm input power level. The high-level input signals normally are handled by switching the amplifier out of the receive line.

Although complicated, the parametric amplifier continues to be the best choice from a low-noise viewpoint. If an ultra-low-noise figure is not required, the bipolar amplifier is the prime candidate below 6 GHz. Between 1975 and 1979, the FET amplifier will be the prime candidate above approximately 6 GHz if its reliability can be demonstrated.

Exciter design considerations.—The primary function of the exciter is to provide a coherent low-noise drive for the transmitter oscillator (TO) and a receiver LO signal to heterodyne the received target returns to an intermediate frequency. The requirement for a stable centerline with low close-in noise dictates that any generation scheme begin with one or more very-high-frequency (vhf) crystal oscillators.

The exciter configuration also varies depending on the type of pulse compression waveform selected. The tradeoffs involve not only the compression ratio but also the method of generation; that is, analog or digital.

The exciter power-level requirements are determined mainly by the type of transmitter selected. Tube-type systems require approximately a 100-mW range for TO drive and a 20-mW range for LO drive. Power levels as much as 500 mW are required for all solid-state designs. Exciter configurations presently in production vary from the all-varactor multiplier-chain type to the high-frequency up-converter type.

The prime candidate for the proposed radar is the basic up-converter configuration shown in figure 5–65. The stable pump source is typically a Gunn or transistor voltage-controlled oscillator harmonically locked to a vhf crystal oscillator. The reference generator provides the signal to be up-converted, generally at a frequency of two to three times the required output bandwidth. This signal can be programed by a vhf synthesizer to provide frequency hopping. The generator can also be designed to provide active chirp or translate a passive pulse compression waveform. This signal can be gated easily to

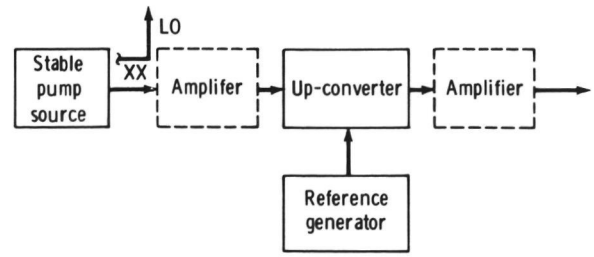

FIGURE 5–65.—Up-converter exciter configuration.

eliminate TO interference on receive. To obtain the required output drive, a Gunn or transistor amplifier must be used either in the pump port or in the output port.

Pulse-compression considerations.—Pulse compression is a means of reducing the peak power required of the transmitter while maintaining the necessary range resolution. Reduction of transmitted peak power has the attendant advantages of lower operating voltages, implying reduced size and weight and increased reliability; and the reduction eases rf breakdown problems throughout the high-power portion of the microwave circuitry. However, peak-power reduction has the disadvantage of having range side lobes that must remain low; otherwise, the background clutter that these side lobes cause will become objectionable.

Pulse-compression technology is highly developed and presents little technical risk in meeting the range of requirements anticipated for the Space Shuttle radar. The available waveforms may be divided into two major categories: (1) analog waveforms of which chirp (linear frequency modulation (FM)) is the most common, and (2) phase-coded waveforms.

The choice of compression ratio is a tradeoff between the desire for low peak transmitted power and the desire to minimize the pulse-compression system complexity.

Range side-lobe performance is another important factor in choosing the compression ratio. Good peak side-lobe performance is difficult to obtain at very low compression ratios ($<13:1$). At high compression ratios, the far-out side lobes cause concern because compressed pulses generally have a side-lobe "plateau," typically 30 to 35 dB below the main lobe, that extends to $\pm\tau$ from the main lobe, where τ is the transmitted pulse width. High-pulse-compression ratios thus lead to a wide plateau and reduced image quality. This phenomenon occurs for both analog chirp and phase-coded waveforms.

Range side-lobe performance: Good range side-lobe performance is required for mapping applications. Typical requirements are that close-in side lobes be 25 dB down from the main lobe and that far-out side lobes be 30 to 35 dB down.

Chirp systems provide good side-lobe performance if frequency weighting is used on receive. A small mismatch loss is incurred (approximately 1.2 dB for 35-dB first side lobes in the absence of errors). The mismatch loss can be eliminated by using nonlinear FM at the expense of increased difficulty in implementation.

Side lobes of phase-coded waveforms depend strongly on the particular code used. Simple-frequency weighting is generally ineffective, but some side-lobe reduction can be obtained by weighting the taps on a tapped-delay line compression filter. As in the case of linear chirp, there is a penalty in signal-to-noise ratio. A tradeoff occurs between implementation complexity and side-lobe performance. Figure 5–66 indicates that binary codes, which have the simplest implementation, have only moderately low side lobes. Polyphase codes have lower side lobes but require more complex implementation.

Reduction of range side lobes in a binary phase-coded system can be effected by transmitting complementary codes on alternate PRF's. In this system, the range side lobes for a zero-Doppler return pulse average to zero. The cancellation is imperfect for

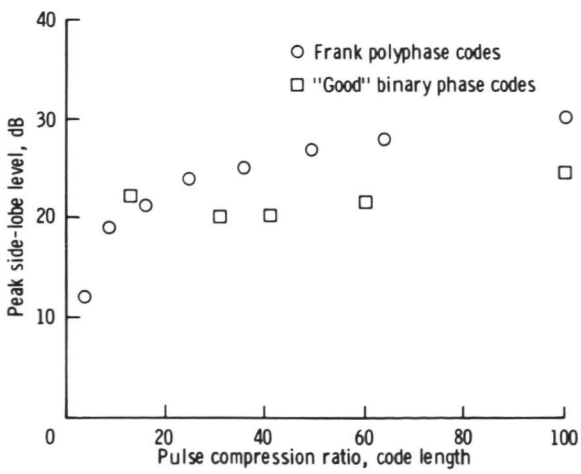

FIGURE 5–66.—Side-lobe levels for phase-coded pulse compression waveforms.

Doppler-shifted targets, but a significant overall improvement in side-lobe level is still obtained.

Generation of the transmitted waveform: The binary phase codes are easiest to generate, requiring only a biphase modulator in the drive signal path to the transmitter. Polyphase codes require a somewhat more complex coder, the complexity depending on the length of the code.

Chirp waveforms can be generated in an analog fashion or in an approximate fashion by using a stepped-phase approximation. In the latter instance, the coder is similar to that used for polyphase codes. Recent studies indicate that the side-lobe performance of the phase-coded approximation is very respectable.

Analog generation is usually somewhat more complex, particularly when frequency agility and coherency are required; polyphase codes are recommended for the Space Shuttle radar system.

COMBINED RAR AND SAR IMAGING

The conventional imaging radar system uses the side-looking geometry. There are other active microwave imaging systems, including the microwave hologram radar and active scanning systems, that can provide imagery from different aspects or look directions.

Down-looking radar systems have a geometry that is identical to that of an IR system or aerial camera. The microwave hologram radar system uses the synthetic aperture technique to realize along-track resolution (refs. 5–12 and 5–13), and crosstrack resolution is obtained by using a phased array antenna (i.e., a real antenna aperture) (refs. 5–14 and 5–15). Microwave hologram radars can be operated in a continuous-wave mode (as compared to pulse transmissions of conventional radars); hence, the range resolution of the conventional radar is replaced by the angular resolution of the phased array antenna. An example of a microwave hologram system is illustrated in figure 5–67 (ref. 5–16). A microwave hologram radar must be designed for operation at the shortest wavelength possible if fine crosstrack resolution is to be realized.

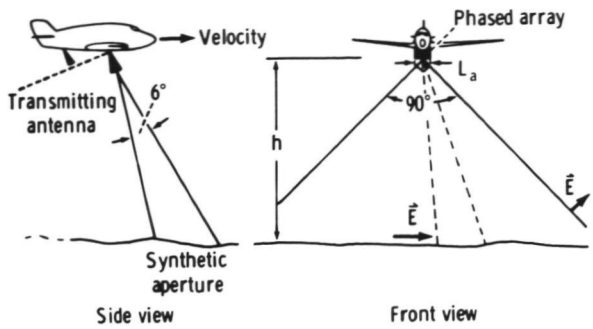

FIGURE 5–67.—Hologram radar geometry (L_a=azimuth length; **E** is the electromagnetic vector).

Basic requirements for the construction of a hologram are that the radiation is sufficiently coherent, that the scattered wavefront received from the image is adequately sampled in two dimensions, and that the sampled wavefront is recorded as wave-transmittance variations on a surface that is an image of the aperture.

Each antenna element has a 90° crosstrack beamwidth (45° each side of vertical when the aircraft is level) and a 6° along-track beamwidth (fig. 5–67). A single transmitting element located behind the receiving array illuminates the terrain. Variations in aircraft velocity are compensated for by varying the velocity of the recording film. This technique was the only motion compensation used in the existing experiment system built by the Environmental Research Institute of Michigan (ERIM).

Both the receiving array and the transmitting antenna are directed forward of the vertical to avoid persistent receiver saturation from very strong specular backscatter signals. The forward squint angle most commonly used has been 12° (a 30° angle was used for one ERIM flight). Backscatter energy from the field of view is compared with a reference frequency in each of the 100 receivers, and the phase-detected outputs are multiplexed into a CRT display which exposes a photographic film. In each dimension, the pattern thus recorded is a hologram

of the microwave frequency "view" from the aircraft. A model of the backscattered microwave signals can be reconstructed with optical waves, which then produces an image of the area viewed.

For nearly vertical viewing, the theoretically achievable resolution in the along-track synthetic aperture direction is given by

$$\rho_x = \frac{\lambda}{4 \sin (\theta/2)} \qquad (5\text{–}27)$$

where θ is the real antenna beamwidth in this direction. Theoretical resolution in the crosstrack phased array direction is given by

$$\rho_y = A \frac{\lambda}{L_a} h \sec^2 \theta_y \qquad (5\text{–}28)$$

where A is a constant of the order of unity that depends on the aperture weighting, L_a is defined in figure 5–67, θ_y is the angle measured from the vertical, and h is the altitude above ground level.

Because the image is three dimensional, direct visual viewing of the relief can theoretically be accomplished. However, because the scaling factors from microwave to light space could not be used in the present experimental system, severe distortions and minor aberrations occur in the reconstructed image. The experimental system does not provide positive indications of terrain relief through use of a mode that causes lines of constant slant range R_1 corresponding to transverse angle θ_1 to appear on the terrain image (fig. 5–68). In this mode, two microwave frequencies are transmitted and the signals from regularly spaced range intervals interfere. The range contour interval is given by

$$\Delta R_c = \frac{c}{2 \Delta f} \qquad (5\text{–}29)$$

where c is the velocity of light and Δf is the difference between the two transmitted frequencies. Slant-range contour lines are not the same as map contour lines. Optical processing for this ranging mode is accomplished in the same manner as for the imaging mode. Radar signal processing can be accomplished by optical or digital-processing techniques.

Similar radar geometry can be realized by using a scanning antenna, scanning in the crosstrack direction and transmitting a pulse-modulated signal to achieve range resolution. Again, the system must be operated at the shortest possible wavelength to realize finest resolution. System designs have been conducted for the application of microwave hologram radars to spacecraft (ref. 5–17).

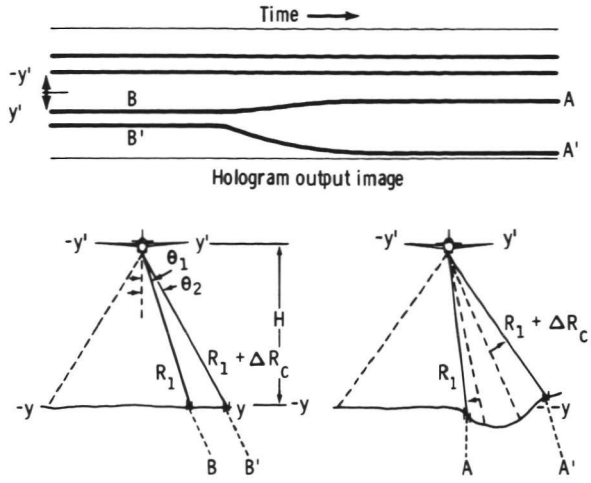

FIGURE 5–68.—Range-contouring geometry for a hologram radar.

Examples of imagery obtained from an experimental microwave hologram radar system are given in figures 5–69 and 5–70. The imagery shown in these figures was obtained by using the parameters shown in table 5–XII.

RADAR SCATTEROMETERS

The following two sections present different aspects of the art of radar scatterometry.

TABLE 5–XII.—*Parameters for Illustrated Imagery of a Hologram Radar System*

[See figs. 5–69 and 5–70]

Altitude, m	300
Swath width, m	[a] 600
Frequency, GHz	16.8
Along-track resolution, m	1.5
Crosstrack resolution, m	6
Contour intervals, m	30

[a] 300 m both sides of nadir.

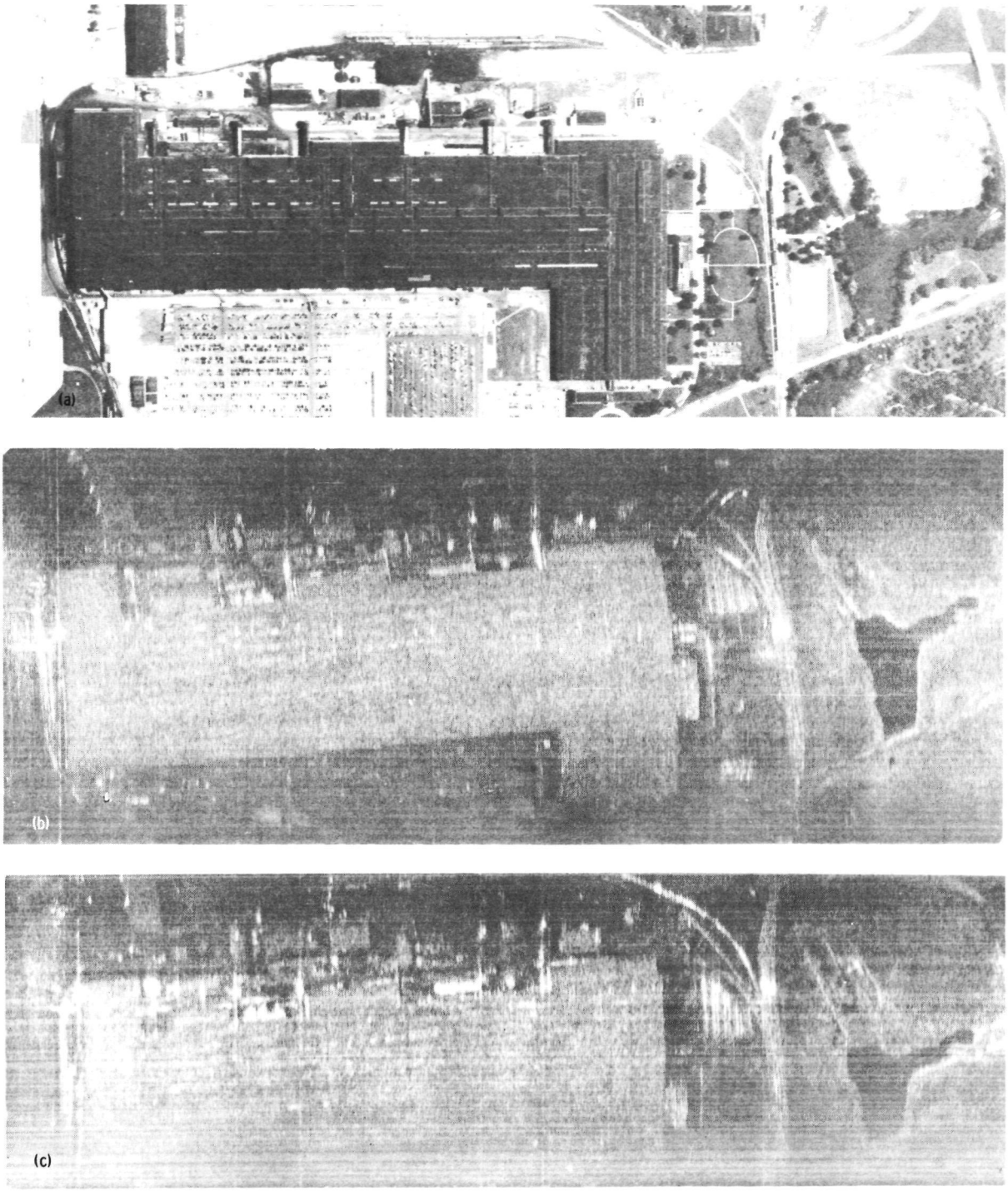

FIGURE 5–69.—Microwave hologram images and a photograph of Willow Run Airport at General Motors Plant. (*a*) Photograph of Willow Run Airport. (*b*) Microwave hologram image of Willow Run Airport; continuous wave operation, 4-mW average power. (*c*) Microwave hologram image of Willow Run Airport; continuous wave operation, 100-mW average power.

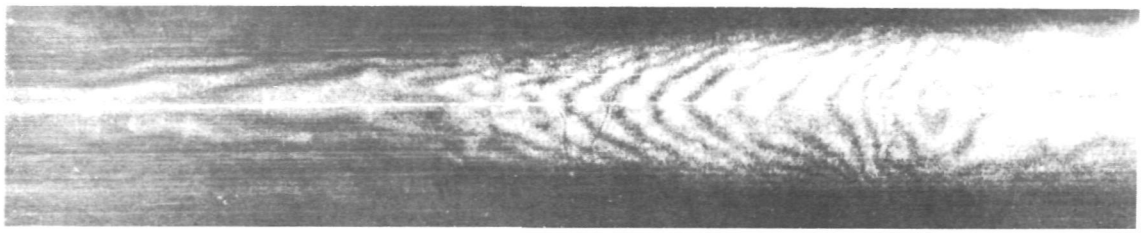

FIGURE 5–70.—Microwave hologram of hill west of Chattanooga, Tenn. (maximum altitude, 520 m; minimum altitude, 300 m).

The first section describes the two basic types of scatterometers, and the second section discusses the different modes of operation and previous experience with radar scatterometers as spacecraft and aircraft sensors.

Radar Scatterometry Design Considerations

Radar measurements have been useful in remote-sensing applications because of the capability to infer from them many characteristics of a target such as range, relative velocity, geometric form, and material composition. A microwave scatterometer is a special-purpose radar used to quantitatively measure only the target reflectance or scattering coefficient. In general, microwave scatterometers are simpler than conventional radars because range and velocity measurement capability and the high spatial resolution (short pulse) requirements are eliminated.

Long-pulse (beam limited) scatterometers have been used to measure the scattering signatures of rough surfaces such as the terrain or the ocean. The quantity of interest is the normalized radar cross section σ°, which is the backscattered power per unit area normalized for antenna gain, range loss, and the transmitted power. In the beam-limited mode, the return in a given range cell comes simultaneously from many scatterers over the entire antenna footprint; therefore, the radar return can be interpreted by using the methods of statistical analysis. To assure antenna-beam-filled conditions, the pulse length τ must satisfy the criterion

$$\tau > \frac{2H\beta}{c \cos \theta_i} \qquad (5\text{–}30)$$

where H is altitude, β is antenna half-power beamwidth (total angle), c is speed of light, and θ_i is surface angle of incidence.

Pencil antenna beam scatterometer.—A simplified block diagram of a microwave scatterometer that uses a narrow-beam antenna is given in figure 5–71. This type of instrument typically operates in a long-pulse or ICW mode (i.e., the receiver is cut off only during the pulse transmission period). The received pulses are shifted in center frequency by the Doppler effect of target and instrument platform motion and have a continuous power spectrum over a finite bandwidth because of the Doppler frequency spread across the antenna footprint. The received signals are down-converted, amplified, narrow-bandpass-filtered, square-law-detected, and integrated.

The normalized radar cross section of the surface can be found from the conventional radar range equation

$$\sigma^\circ = \frac{P_r (4\pi)^3 R_s^4}{P_t G^2 \lambda^2 A} \qquad (5\text{–}31)$$

where P_r is power in return pulse, P_t is

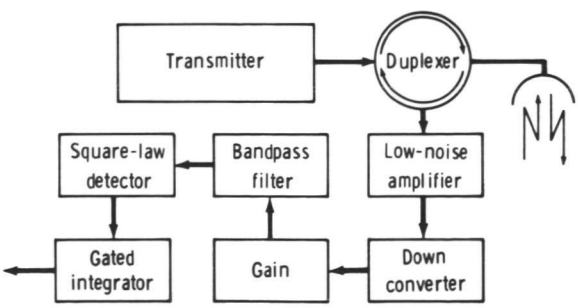

FIGURE 5–71.—Simplified block diagram of a microwave scatterometer that uses a narrow-beam antenna.

power in transmitted pulse, R_s is slant range to illuminated area, λ is free space wavelength, A is effective illuminated area (antenna footprint), and G is antenna gain. For the case of a beam-limited scatterometer at satellite altitudes (where curved Earth effects are important), the normalized radar cross section is

$$\sigma^\circ = \frac{P_r (4\pi)^2 H^2 L_{\text{atm}}^2 \cos\theta_i}{P_t G \lambda^2 (1-k)^2 \cos^2\phi\eta} \qquad (5\text{–}32)$$

where H is satellite altitude, L_{atm} is one-way atmospheric power loss factor, θ_i is Earth incident angle, k is $H(\tan^2\phi)/2R_E$, R_E is Earth radius, ϕ is nadir angle, and η is antenna efficiency $=(G\beta^2)/(4\pi)$. Because of the antenna-beam-filled conditions, the antenna gain appears as the first power, and the altitude (range) is squared; whereas, in the generalized radar range equation, the gain is squared, and range is to the fourth power.

Unfortunately, the output voltage from the square-law detector is corrupted by rectified received antenna noise. A gated ideal integrator is used to average the detector output for several return pulses, yielding a measurement of signal plus noise. This measurement is followed by an integration of noise alone (square-law detector output in the absence of return pulses). The subtraction of these measurements yields an estimate of the received power.

The form of the radar equation appropriate to the design of a scatterometer is

$$(S/N)_{\text{in}} = \frac{P_t G \lambda^2 \sigma^\circ \cos^2\phi\eta}{(4\pi)^2 H^2 \cos\theta_i L_{\text{atm}}^2 L_s^2 K T_s B_{\text{if}}} \qquad (5\text{–}33)$$

where $(S/N)_{\text{in}}$ is input signal-to-noise ratio, L_s is system power loss factor, k is Boltzmann constant, T_s is system noise temperature, and B_{if} is predetection intermediate frequency bandwidth. The precision of the scatterometer measurement is

$$\frac{\Delta\sigma^\circ}{\sigma^\circ} \approx \left[\frac{1}{B_{\text{if}}\tau_{s+n}}\left(1+\frac{1}{(S/N)_{\text{in}}}\right)^2 + \frac{1}{B_{\text{if}}\tau_n}\left(\frac{1}{(S/N)_{\text{in}}}\right)^2\right]^{1/2} \qquad (5\text{–}34)$$

where $\Delta\sigma^\circ/\sigma^\circ$ is normalized standard deviation in measuring σ°, τ_{s+n} is total integration time of noise-contaminated signal, and τ_n is total integration time for noise alone.

Figure 5–72 is a plot of $\Delta\sigma^\circ/\sigma^\circ$ as a function of $(S/N)_{\text{in}}$ for various integration times, where τ_{s+n} is assumed equal to τ_n. The intermediate frequency bandwidth B_{if} is 11 kHz and is assumed to be approximately the Doppler spread and equal for the "signal-plus-noise" and "noise-alone" measurements. A sufficient integration yields good measurement standard deviations for negative $(S/N)_{\text{in}}$.

A sample link calculation for a typical high-inclination-orbit satellite is given in the section entitled "A Shuttle Radar Microwave Subsystem for Earth Resources Applications." The total transmit/receive cycle is assumed to be 21 msec (PRF of approximately 47 pulses/sec) with an idealized 33.3-percent transmitter duty cycle. The integration time required for the σ° measurement was based on $\sigma^\circ_{\text{min}} = -30$ dB and on $\Delta\sigma^\circ/\sigma^\circ = 50$ percent. Because the signal-plus-noise integration period is 33.3 percent of the transmit/receive cycle, the required measurement time t_m is equal to 3τ. For applications in which large ground coverage is required, the maximum allowable measurement (integration) time is based on the antenna slew rate and the allowable smear (caused by platform motion) of the antenna footprint.

Fan-beam antenna scatterometer.—The operation of a fan-beam antenna microwave scatterometer is equivalent to several simultaneous pencil-beam systems. The effective multiple pencil-beam operation is achieved by filtering the Doppler-shifted radar return to subdivide the broad beam into an arbitrary number of resolution cells. A simplified block diagram is shown in figure 5–73. The system is beam limited in each Doppler cell, although it may not be beam limited simultaneously over the entire fan beam. Because of differences in slant range across the antenna footprint, separate range gates are required for each channel.

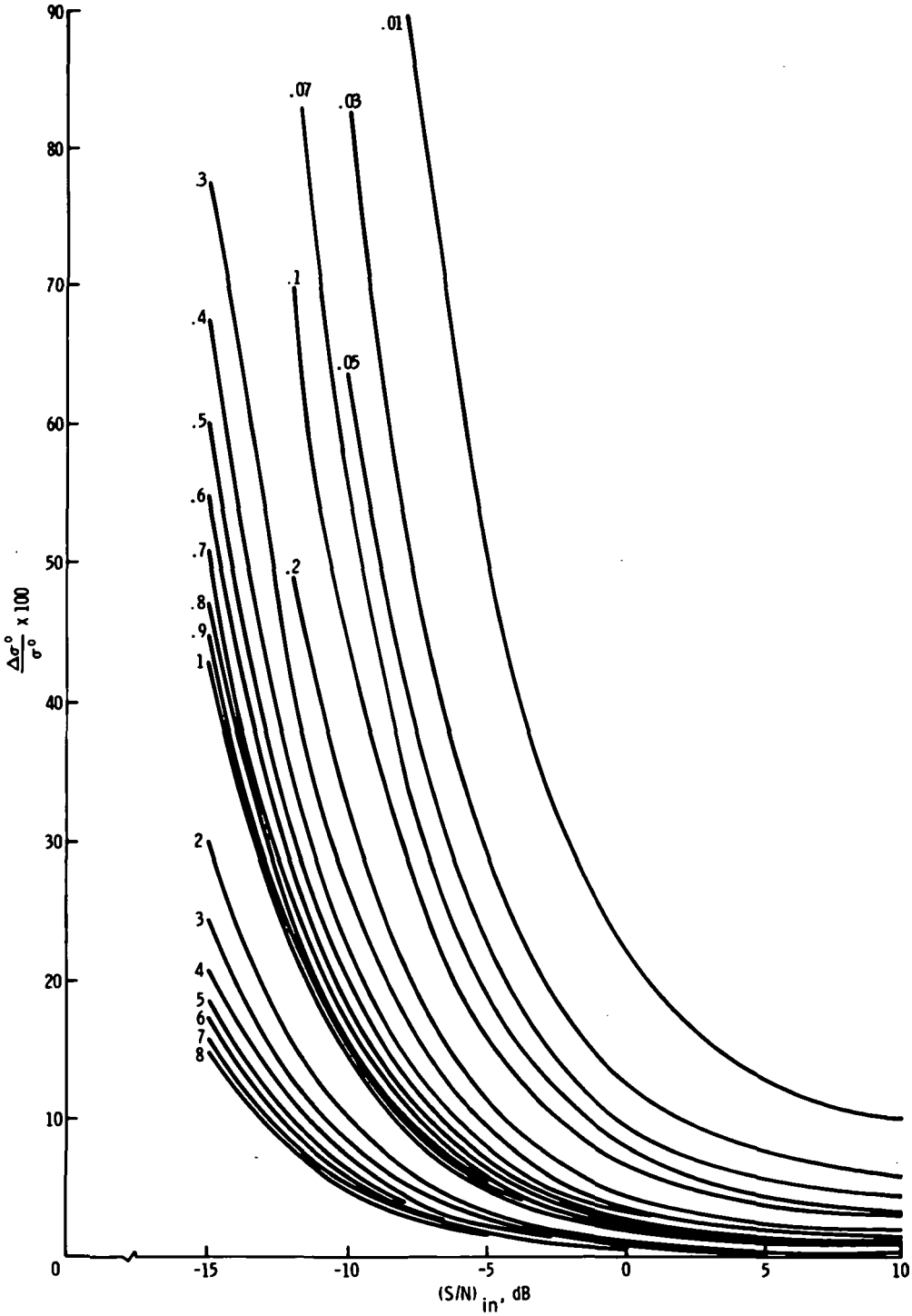

FIGURE 5-72.—Plot of $\Delta\sigma^\circ/\sigma^\circ$ as a function of $(S/N)_{in}$ for integration times indicated; τ_{s+n} is assumed equal to τ_n; the intermediate frequency bandwidth B_{if} equals 11 kHz and is assumed to be approximately the Doppler spread.

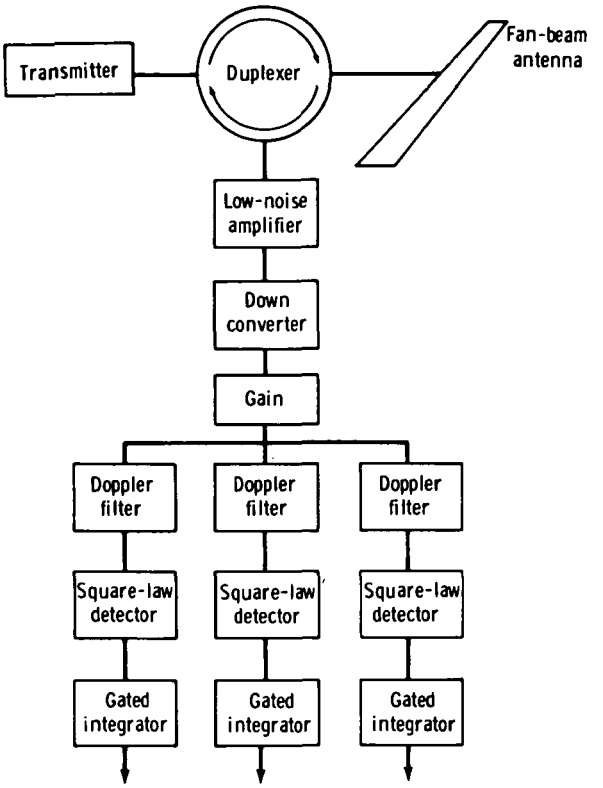

FIGURE 5–73.—Simplified block diagram of a fan-beam microwave scatterometer.

The equations used for this scatterometer are essentially identical to those used for the pencil-beam instrument. However, corrections must be made for differences in slant range, antenna gain, and effective beamwidth for each fan-beam receiver channel. Because of the multibeam aspects of the fan-beam instrument, the equivalent ground coverage (relative to a pencil-beam scatterometer) can be achieved with lower antenna slew rates, and, in some instances, without slewing the antenna at all. This characteristic results in longer available integration times and, thus, lower transmitter power requirements. However, the increase in transmitter power to compensate for the loss in the fan-beam antenna gain is greater than the savings. The system parameters for a satellite fan-beam scatterometer (to give the equivalent performance as the pencil-beam system described earlier) are P_t of 125 W, PRF of 74 pulse/sec, number of Doppler channels is 20, and antenna beamwidth is 0.5° by 20°.

Radar Scatterometry Applications

Radars capable of measuring backscattering cross sections from ocean or land have been generally referred to as scatterometers (ref. 5–18). Such systems may use continuous wave (CW) signals with or without Doppler processing or FM and pulse techniques.

A CW scatterometer depends on its antenna to distinguish among returns from various angles. The capability of radar to separate returns from different ranges can be used advantageously together with directive antenna beams to simplify the scattering measurements (ref. 5–19). A fan beam can be used to illuminate a narrow strip along the ground, and the range resolution permits separation of signals from different angles.

Another way to measure a scattering coefficient is to use Doppler bandwidths corresponding to a resolution cell on the ground. In such systems, a CW signal is transmitted. Contractors have built CW Doppler radars for various NASA programs (refs. 5–20 to 5–22).

The 0.4-GHz scatterometer and the 13.3-GHz scatterometer are similar. In both systems, a fan-shaped beam (fig. 5–74) il-

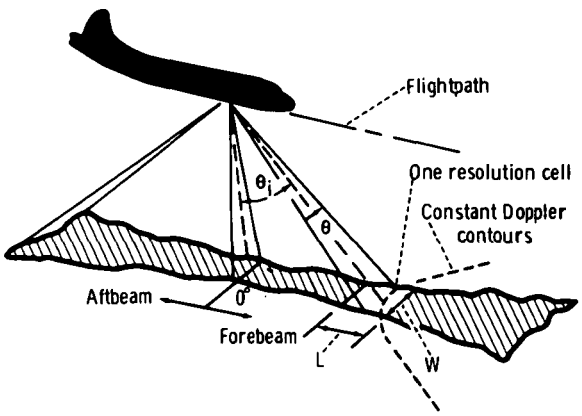

FIGURE 5–74.—The 13.3-GHz scatterometer resolution cell geometry; θ is radar beamwidth, θ_i is incidence angle, L is resolution cell length, and W is resolution cell width or $f(h, \theta_i, \theta)$.

luminates the ground. Doppler frequencies are used in digital processing to separate returns from various resolution cells. In the 0.4-GHz scatterometer, an intermediate frequency is used to record returns from −60° to 60° on a positive frequency axis. However, in the 13.3-GHz scatterometer, a zero intermediate frequency is used, and returns corresponding to fore-and-aft beams are separated by using a sign-sensing technique. In this section, the details of the 13.3-GHz NASA aircraft scatterometer and the Skylab S193 13.9-GHz scatterometer are discussed. This discussion concludes with future hardware recommendations.

The NASA Lyndon B. Johnson Space Center 13.3-GHz scatterometer.—A circuit diagram of the 13.3-GHz system is shown in figure 5–75. The microwave energy is radiated by an antenna that has wide fore-and-aft beams and a narrow transverse beam. The returned energy may be separated using the Doppler equation as a function of incident angle:

$$f_d = \frac{2v}{\lambda} \sin \theta_i \qquad (5\text{–}35)$$

where f_d is Doppler frequency, v is aircraft ground velocity, λ is wavelength of the transmitted power, and θ_i is angle of incidence.

The returned energy is received simultaneously from all incident angles and is divided equally into two channels, one of which is 90° out of phase with the other. The data for each channel, detected by a direct-to-audio technique, are amplified and recorded on an FM tape recorder. The fore-and-aft-beam data are separated by use of a sign-sensing technique. To calibrate the system, a ferrite modulator is used to provide an absolute power reference level of the transmitted signal. The σ° as a function of θ_i information is obtained by subtracting known system losses and aircraft altitude and velocity factors and by comparing the remainder with a reference signal level.

Skylab S193 radiometer/scatterometer.—The Skylab S193 radiometer/scatterometer (RADSCAT) sensor consists of a combina-

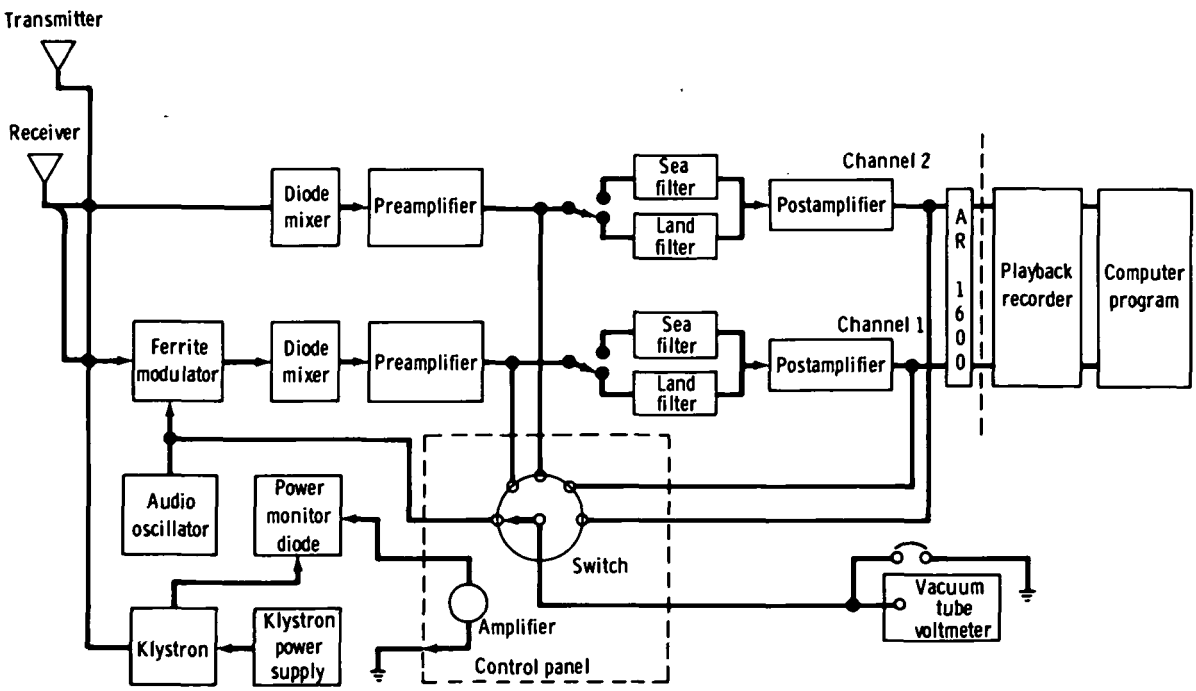

FIGURE 5–75.—Block diagram of 13.3-GHz scatterometer system.

tion of active and passive microwave sensors designed to perform scientific experiments to study the Earth from space.

The radiometer measures the radiometric brightness temperature from areas on the surface of the Earth as a function of incident angle in the interval of frequencies from 13.8 to 14.0 GHz. The mean value of the thermal noise signal of the Earth is compared to the measured mean noise signal of two known temperature sources to yield a precise measurement of the emission temperature of the resolution cell of the Earth. The brightness temperatures for both vertical and horizontal polarizations can be measured with the Skylab S193 radiometer.

The scatterometer measures the backscattering cross sections of an illuminated area on the Earth. The incident energy can be radiated with horizontal or vertical polarization. Corresponding to each incident polarization, both vertically and horizontally polarized backscattered energy can be measured. The angles of incidence range from 0° to 52°.

The radiometer and scatterometer can operate both jointly and separately in various scanning and polarization modes. A summary of these modes follows.

In-track noncontiguous mode: The in-track noncontiguous (ITNC) mode is used for a joint radiometer and scatterometer operation. In this mode, only the pitch angle is varied. A resolution cell on the ground (fig. 5–76) is seen by the radiometer and

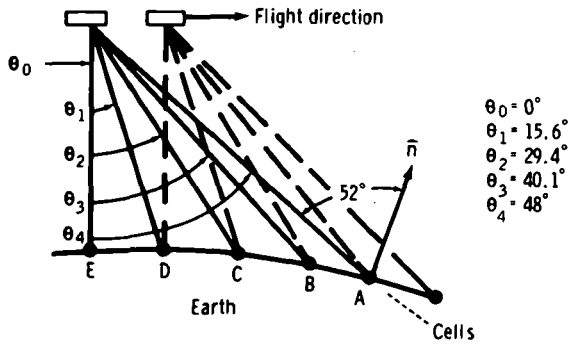

FIGURE 5–76.—The RADSCAT ITNC scanning mode with varied pitch angle θ; **n** is local vertical vector.

scatterometer at approximately the following pitch angles: 0°, 15.6°, 29.4°, 40.1°, and 48°.

During each dwell at a given pitch angle, the following measurements are taken:

1. Scatterometer data with vertical transmit/vertical receive (VV), horizontal transmit/horizontal receive (HH), vertical transmit/horizontal receive (VH), and horizontal transmit/vertical receive (HV) polarizations.
2. Radiometer and noise data with vertical and horizontal polarizations.
3. Radiometer reference voltages (R_1 for calibration and R_2 as baseline).

The measurement sequences are shown in figure 5–77. In this mode, the roll angle is always zero.

Crosstrack noncontiguous mode: In the crosstrack noncontiguous (CTNC) mode, the roll angle is varied identically to the ITNC mode, and the pitch angle remains zero. The motion of the field of view is shown in figure 5–78, in which individual cells are viewed from only one antenna position. Because of the motion of the antenna in the pitch direction, the cells lie on a curved arc. As shown in the figure, there are three forms of this mode: left scan, right scan, and left/right scan. The outermost cell is viewed at approximately 52° (corresponding to a 48° gimbal angle), and the innermost cell, at approximately 0° at all times.

The sequence of measurements is shown in figure 5–77. Only combined RADSCAT data can be gathered in the CTNC mode. In the sequence mode, data for all polarization combinations are gathered automatically for radiometer and scatterometer systems.

In-track contiguous mode: The pattern of the in-track contiguous (ITC) scanning mode (fig. 5–79) is similar to the ITNC mode, except that the antenna is scanned much faster and no dwell occurs at any antenna pitch angle. The entire in-flight path is eventually scanned at all incident angles with this process.

The scan cycle time is chosen so that at the vehicle velocity, the resolution cell at inci-

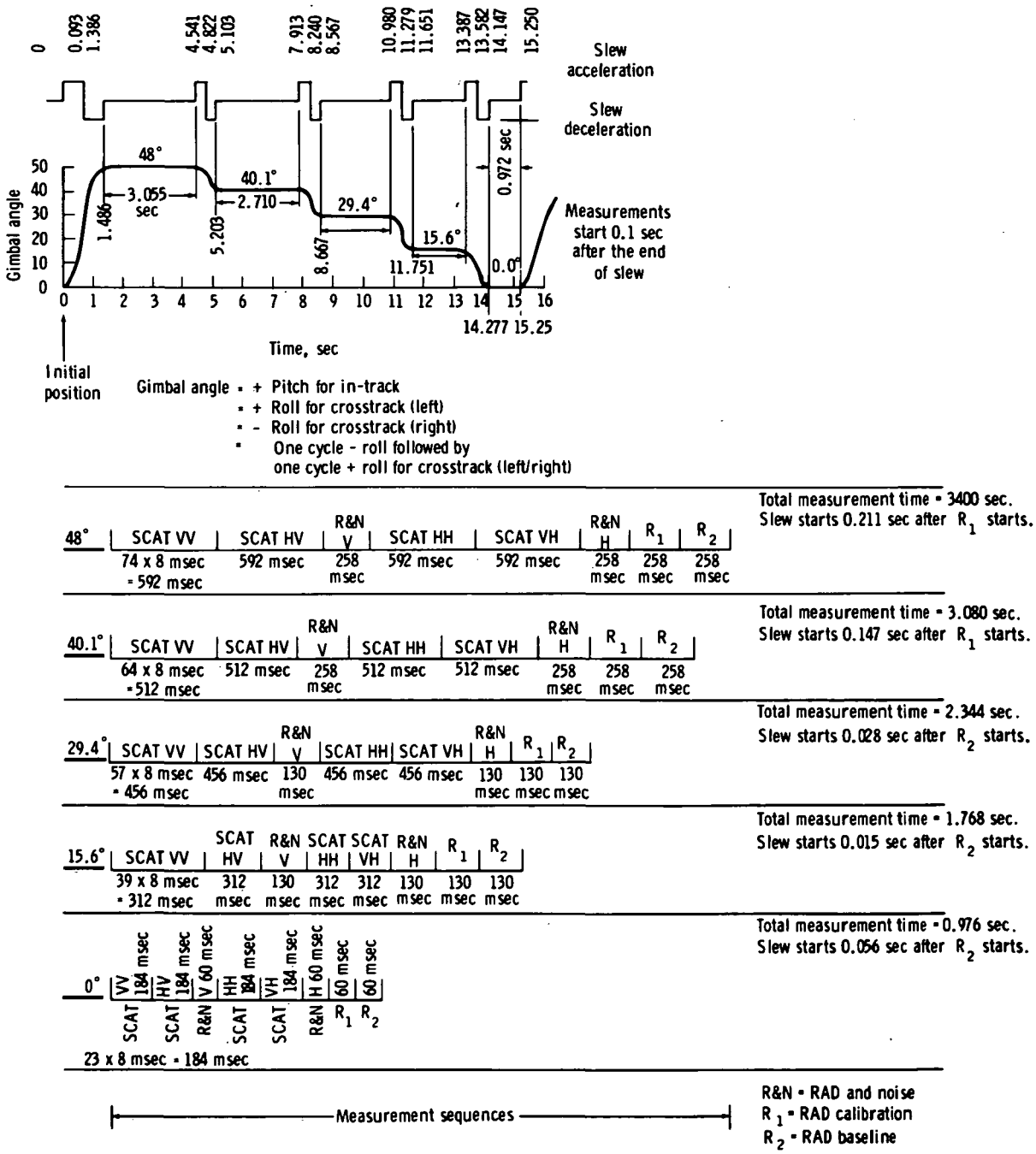

FIGURE 5–77.—Measurement sequence for ITNC and CTNC modes.

dent angle 48° overlaps the previous cell by approximately 25 percent; the 40.1° cell overlaps its predecessor by less than 20 percent, and so forth. At the 0° incident angle, gapping rather than overlap occurs. The measurement sequence is explained in figure 5–80.

The radiometer data are taken during skew periods between two pitch angles corresponding to scatterometer data angles. In

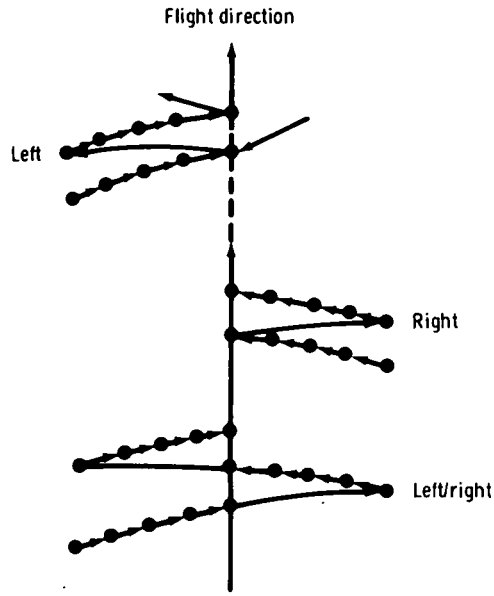

FIGURE 5–78.—Motion of the field of view, CTNC mode.

this mode during a given pass, only one transmitted polarization can be chosen. Data corresponding to the vertical or horizontal polarization are received. As the vehicle progresses on successive scans, the entire path is viewed at 48° and less, except for gapping at the low angles.

Crosstrack contiguous mode: The crosstrack contiguous (CTC) mode contains the following three submodes:

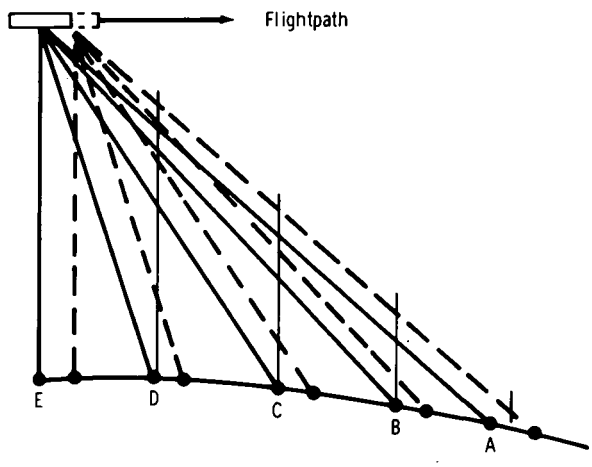

FIGURE 5–79.—The ITC mode.

1. The RADSCAT: In this submode, the astronaut can select one in-phase polarization pair, VV or HH.

2. Radiometer: In this submode, data corresponding to vertical and horizontal polarization are recorded.

3. Scatterometer: In this submode, data for. VV and HH polarization combinations are recorded.

The CTC mode provides a side-to-side linear scan covering ±11.375°. As indicated in figure 5–81, the CTC is a mapping mode. To compensate for the satellite forward velocity, which could cause skewing of the pattern perpendicular to the flightpath, the pitch gimbal is scanned slightly backward as the roll angle oscillates between its limits. Measurements are made for every 1.896° of beam center motion, ranging from −11.375° to 11.375° in roll. The measurement times and sequences are shown in figure 5–82. The pitch offset angles for this mode can be chosen as incident angles of 0°, 15.6°, 29.4°, or 40.1°.

Future research and development.—The performance of NASA 13.3- and 13.9-GHz RADSCAT scatterometers has been fully demonstrated by aircraft and Skylab missions. However, these systems were basically experimental in nature. These programs have indicated a need for improving both hardware and software capabilities. Procedures for collecting the data should be revised for an operational system. The following research and development are recommended:

Improved radar calibration techniques: A calibration period should follow each data-collection period. The frequency of these calibrations will depend on the performance of the system. Some technique of external calibration should be adopted. Corner reflectors over smooth deterministic targets can be used for airborne and spaceborne scatterometers. Internal calibrations are undesirable because they do not involve all paths that the actual returned energy traverses.

Improved systems design: Improvements

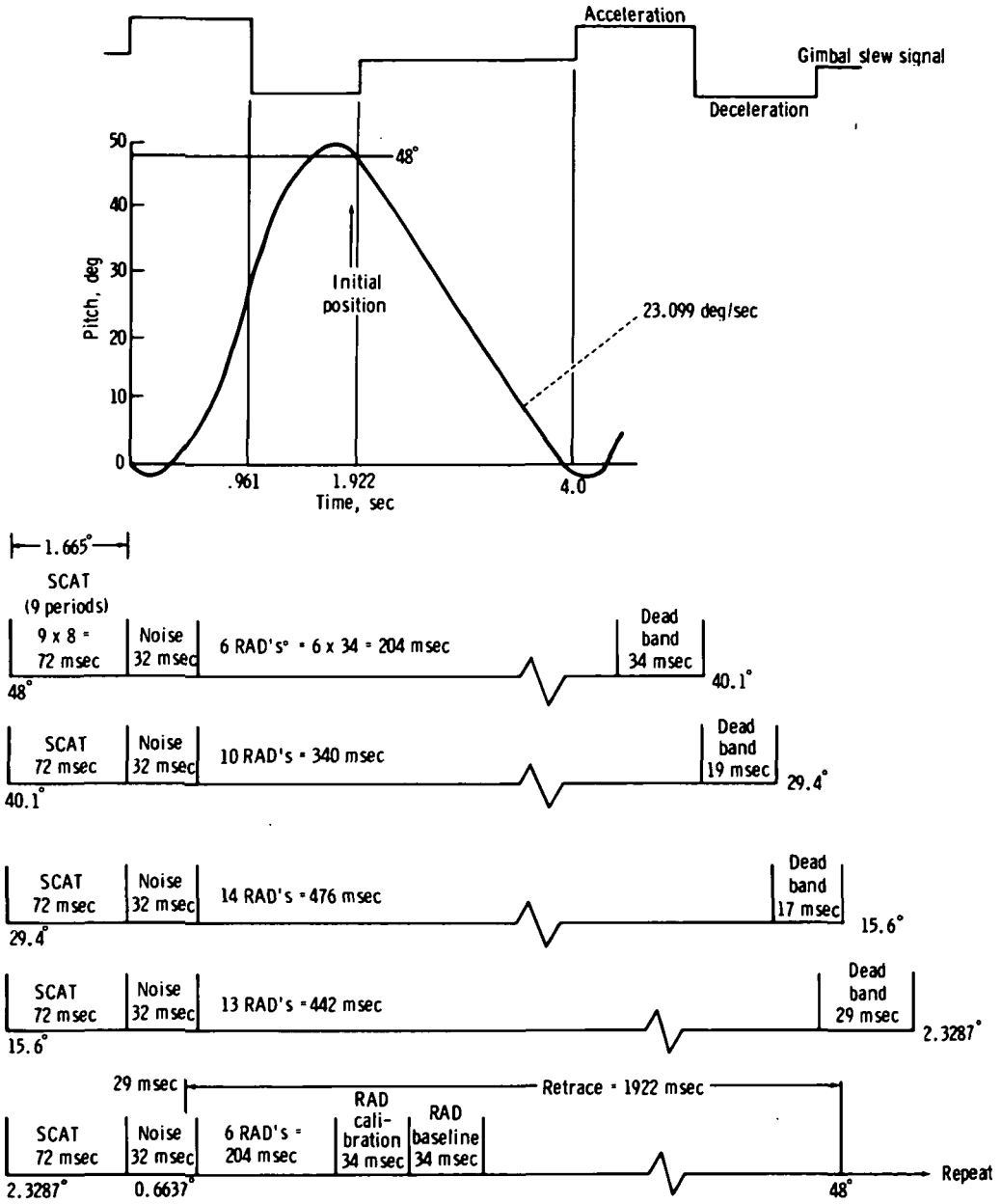

One selected polarization pair from VV, VH, HV, and HH (Example: HV means: SCAT transmit = H; SCAT receive and SCAT noise and RAD = V).
*Each radar measurement period is 32 msec plus 2 msec readout.

FIGURE 5–80.—Measurement sequence for the ITC mode.

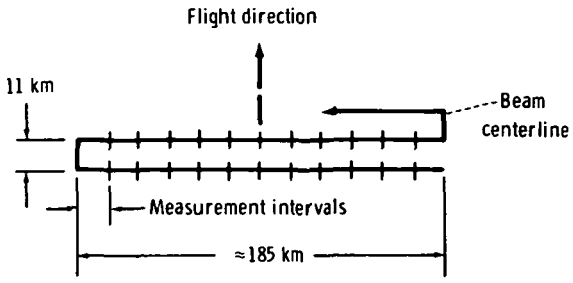

FIGURE 5–81.—The CTC mode.

are needed in the reliability of the antenna gimbaling, switching logic, and polarization isolation. System drifts, resolution, and noise-level fluctuations have to be reduced in future airborne and spaceborne systems.

Data-processing techniques: For operational systems, highly efficient data-processing techniques are needed; no reliable data-display techniques have been advanced to date. Onboard processing of data should be explored, and the digitally processed data should be color coded to display ocean winds and waves for visual interpretation and use. These programs should be capable of handling large volumes of reflectivity data and displaying these data on a world map.

Calibration data measurements: For spaceborne and airborne instruments, the calibration data corresponding to each subsystem are usually measured in the laboratory. The amplifier, mixer, and filter gains are some examples. For instruments flown for extended periods, these internal gains change. To alleviate this problem, automatic calibration modes should be designed to check all calibration data needed to calculate backscattering cross sections from raw data.

Applicability.—Multifrequency, multipolarization scatterometers can be used to measure winds and waves at the surface of the ocean and to detect development and progress of storms. These surface measurements can be used to predict weather and to forecast storm developments. Sea-state forecasting will aid in the navigation and routing of ships.

SUBSURFACE SOUNDERS

This section is concerned with airborne or spaceborne electromagnetic systems used to detect subsurface features.

The skin depth of a wave propagating into the ground, defined as the depth at which the electromagnetic field decays to e^{-1} of its value at the surface, is given by

$$\delta = \left(\frac{2\rho}{\mu_0 \omega}\right)^{1/2} \qquad (5\text{–}36)$$

where ρ is resistivity of the ground material (ohm-m), μ_0 is magnetic permeability of free space (H/m), ω is angular frequency $=2\pi f$, and f is frequency of the electromagnetic wave (Hz). Resistivities for normal ground rank between 10 ohm-m for clay soil to 3000 ohm-m for gravel and rock (ref. 5–23). To sound such ground to any appreciable depth, very low frequency (vlf) will have to be used. At 10 kHz, a skin depth of approximately 15 m will result for a ground with a 10-ohm-m resistivity, for example. With a resistivity of 1000 ohm-m, the corresponding skin depth is 150 m. At a frequency of 100 MHz, the skin depths are 0.15 and 1.5 m for the same resistivities.

The resistivities vary with the content of water and with the temperature. In permafrost regions, the ice contained in the ground may cause resistivities of approximately 100 000 ohm-m.

Radio-Wave Method

Soundings at a vlf with active devices are impractical because of interference from radio transmitters with signals that are propagated over very long distances along the surface of the Earth. However, one may take advantage of these vlf signals for investigation of subsurface features by using the so-called wave-tilt method. At a given position at the ground (fig. 5–83), the vertically polarized radio surface wave radiated from a vlf station may be resolved into the three components shown. The ratio between the longitudinal and the vertical electrical components is the wave tilt, which is dependent on the resistivity of the ground.